

# Performance of cryogenic silicon microstrip detectors at the COMPASS experiment

Diploma thesis  
by  
Philipp Zimmerer

TECHNISCHE UNIVERSITÄT MÜNCHEN  
Physik Department E18



### **Abstract**

In 2009, the silicon microstrip detectors at the COMPASS experiment were for the first time operated permanently in a cryogenic state with a temperature of 200 K both as a beam telescope and as a vertex detector. The main purpose of this modification was to diminish the damage the detectors suffer from irradiation from the high-intensity beam. At the same time, a significant improvement in time resolution could be achieved while spatial resolution and efficiency were not affected.



# Contents

<b>1</b>	<b>Introduction</b>	<b>1</b>
<b>2</b>	<b>The COMPASS experiment</b>	<b>3</b>
2.1	The physics program of COMPASS . . . . .	3
2.1.1	Physics with hadron beam . . . . .	3
2.1.2	Physics with muon beam . . . . .	5
2.2	Spectrometer setup . . . . .	7
2.2.1	The M2 beam line . . . . .	7
2.2.2	Spectrometer regions . . . . .	8
2.2.3	Detector components . . . . .	9
2.2.4	Specifics for hadron beam . . . . .	10
2.2.5	Specifics for muon beam . . . . .	12
2.3	Readout chain and analysis tools . . . . .	12
2.3.1	Data acquisition . . . . .	12
2.3.2	Cinderella - The online filter . . . . .	13
2.3.3	The ROOT analysis framework . . . . .	13
2.3.4	Online monitoring with COOOL . . . . .	13
2.3.5	COMGEANT spectrometer simulation . . . . .	13
2.3.6	Event reconstruction with Coral . . . . .	14
2.3.7	PHAST - Data analysis . . . . .	15
<b>3</b>	<b>The COMPASS silicon microstrip detector</b>	<b>17</b>
3.1	Working principle . . . . .	17
3.2	The COMPASS silicon detector setup . . . . .	18
3.2.1	Requirements . . . . .	18
3.2.2	Wafer design . . . . .	18
3.2.3	Detector module . . . . .	19
3.2.4	Frontend electronics and readout chain . . . . .	19
3.2.5	The detector stations . . . . .	22

## CONTENTS

3.3	Cold detectors . . . . .	23
3.3.1	Purpose and principle . . . . .	24
3.3.2	Cryogenics . . . . .	24
3.4	Outlook . . . . .	24
<b>4</b>	<b>Data reconstruction for the silicon detectors</b>	<b>29</b>
4.1	Detector signal . . . . .	29
4.2	Time reconstruction . . . . .	29
4.2.1	Signal shape . . . . .	33
4.3	Time Calibration . . . . .	34
4.3.1	"Jumping" time calibrations . . . . .	36
4.4	Clustering . . . . .	38
4.4.1	Finding regions and splitting into clusters . . . . .	38
4.4.2	Cluster position . . . . .	39
<b>5</b>	<b>Performance of the detectors in cryogenic and non-cryogenic operation</b>	<b>41</b>
5.1	Hardware . . . . .	41
5.1.1	Cooling system . . . . .	41
5.2	Tracking performance . . . . .	42
5.2.1	Amplitude and noise levels . . . . .	42
5.2.2	Signal shape and time resolution . . . . .	43
5.2.3	Charge sharing and residuals . . . . .	43
5.2.4	Tracking (Pseudo-)Efficiency . . . . .	48
<b>6</b>	<b>Alignment studies</b>	<b>51</b>
6.1	The alignment procedure . . . . .	51
6.2	z-realignment studies of the conical cryostat . . . . .	52
<b>7</b>	<b>Conclusion</b>	<b>55</b>
7.1	Results . . . . .	55
7.2	Outlook . . . . .	55
<b>A</b>	<b>Time calibration guide</b>	<b>57</b>
A.1	Raw data . . . . .	58
A.2	Coral and PHAST . . . . .	58
A.3	PHAST user event functions . . . . .	60
A.4	Root macros and creating/editing calibrations . . . . .	61
<b>B</b>	<b>Plots and Histograms</b>	<b>65</b>

**Bibliography**

**76**



# List of Figures

2.1	The COMPASS spectrometer in its hadron configuration . . . . .	4
2.2	The Primakoff effect . . . . .	4
3.1	Cross section of the silicon wafer . . . . .	18
3.2	The silicon detector module . . . . .	20
3.3	Readout chain, from [Din11] . . . . .	21
3.4	The CC during its dismount in november 2009 . . . . .	23
3.5	Schematics of the cooling system: valve box and upstream station, from [Bic11] . . . . .	25
3.6	Schematics of the cooling system: conical cryostat, from [Bic11] . . . . .	26
4.1	APV response to a $\delta$ -like input . . . . .	30
4.2	Latency scan of SI03Y in 2010 . . . . .	31
4.3	Signal shape for SI03Y calibrations in 2010 . . . . .	34
4.4	Latency adjustment, from [Wag01] . . . . .	35
4.5	Timing distribution for SI03Y in hadron run 2009 . . . . .	36
4.6	Ratio vs. TCS phase histograms for SI01U in run 77918, displaying jump in timing . . . . .	37
4.7	Distributions of charge fraction $\eta$ . . . . .	40
4.8	Distribution of residuals for SI03Y in run 76860 for cluster sizes 1 and 2 . . . . .	40
5.1	Cluster amplitudes of detector module SI1.08 in cryogenic and non-cryogenic operation . . . . .	42
5.2	Signal shapes for non-cryogenic and cryogenic detectors . . . . .	44
5.3	Timing of the p-side of module SI1.08 in non-cryogenic and cryogenic operation. . . . .	45
5.4	Distribution of charge fraction coefficient $\eta$ for n-sides of different productions . . . . .	46
5.5	Distribution of residuals over charge fraction coefficient $\eta$ . . . . .	46
5.6	Residuals of SI1.08 non-cryogenic and cryogenic operation . . . . .	47

*LIST OF FIGURES*

5.7 Pseudo-efficiency of n-side of SI1.08 in cryogenic and non-cryogenic operation . . . . . 49

6.1 Z distribution of vertices in the target region before and after re-alignment 54

7.1 Amplitude correlation between hits in adjacent planes . . . . . 56

# Chapter 1

## Introduction

The COMPASS experiment at CERN looks to discover new physics and test predictions in the field of spin structure functions of hadrons and chiral perturbation theory, as well as discover new hadronic and exotic states. It is equipped to make use of both hadron and muon beam, fitting the respective requirements of the program. A more detailed overview over the experiment and its physics objectives is given in chapter 2.

The double-sided silicon microstrip detectors are an integral component of the COMPASS experiment in all programs due to their unparalleled spatial resolution of  $\sim 10 \mu\text{m}$ . Because of the high-intensity beam, the detectors are subject to radiation-induced damage and a correlated loss of charge collection efficiency. In order to reduce this damage, the detectors have been operated in a cold state starting 2009. Chapter 3 gives an introduction to the concept of the detectors, its electronic infrastructure and the cooling system.

Chapter 4 describes the reconstruction of hits in the detectors from the produced raw data, where an emphasis is set on the time reconstruction function and its calibration. In chapter 5 a comparison of cryogenic and non-cryogenic operation is issued with the goal to judge whether the technically more complicated cryogenic operation offers improvements over the non-cryogenic operation mode.



## Chapter 2

# The COMPASS experiment

The COMPASS (Common Muon and Proton Apparatus for Structure and Spectroscopy) [Co96] experiment is a high luminosity, fix target experiment at the SPS<sup>1</sup> particle accelerator at CERN<sup>2</sup>. It can make use of both muon and hadron beams, covering a wide field of physics to probe. This chapter discusses the physics potential as well as the spectrometer setup and its variations depending on the running program. It concludes with a summary of the analysis chain of COMPASS.

## 2.1 The physics program of COMPASS

### 2.1.1 Physics with hadron beam

#### Primakoff reactions

While Quantum Chromodynamics (QCD) as a perturbative field theory has been found to describe strong interactions at high energy very well, in the low-energy regime confinement (expressed by a comparatively high value of the strong coupling constant  $\alpha_s$ ) this perturbativity does not hold up any more. On the other hand, Chiral Perturbation Theory (ChPT) has turned out to be a rather good description of the behaviour of hadrons. It makes predictions on basic properties of hadrons, like dipole moments, polarisabilities and lifetimes.

In the Primakoff effect, a high-energetic hadron scatters off the Coulomb field of a target nucleus, described by a quasi-real photon (i.e. a photon with small virtuality  $Q^2$ ). In the process, a hard photon is emitted,  $\pi + {}^A Z \rightarrow \pi' + {}^A Z' + \gamma$ . This effect is sensitive to the polarisability and lifetime of the  $\pi^0$  mass and thus offers tests of ChPT.

---

<sup>1</sup>Super Proton Synchrotron

<sup>2</sup>Le Conseil Européenne pour la Recherche Nucleaire - The European Nuclear Research Organisation

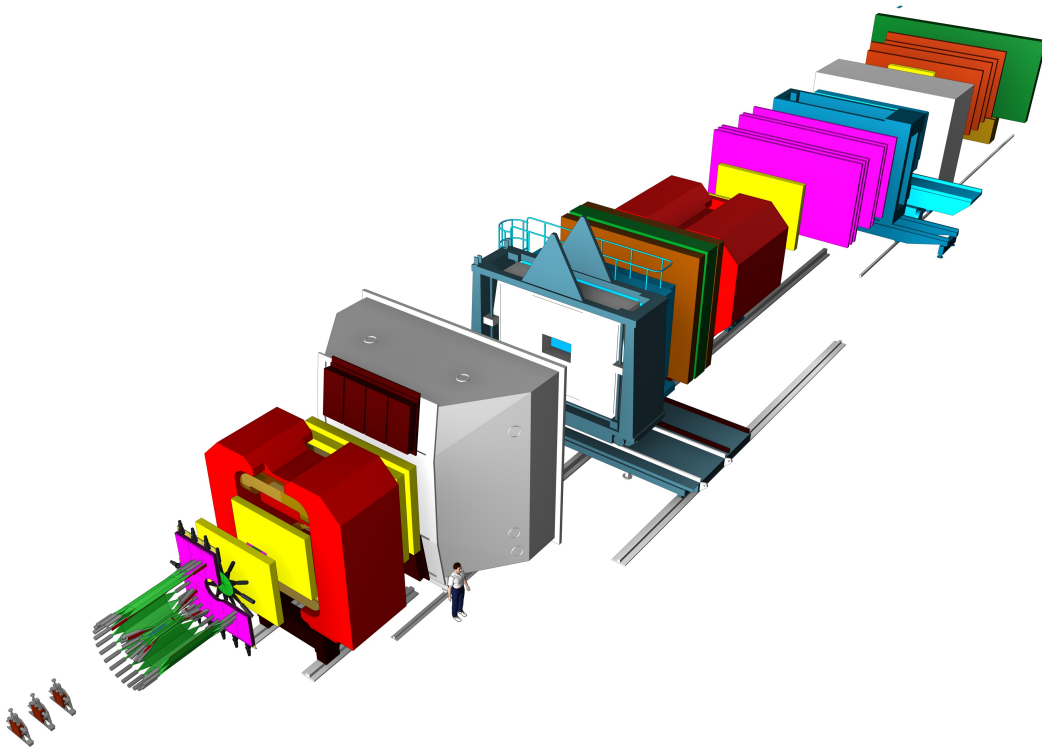


**Figure 2.1:** The COMPASS spectrometer in its hadron configuration

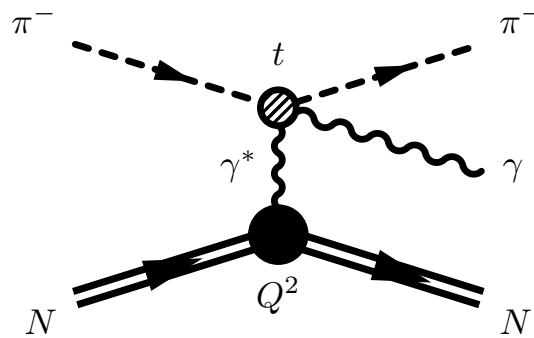


**Figure 2.2:** The Primakoff effect

### Exotic states

The most simple bound quark states in QCD are baryons and mesons, forming a color singlet as a combination of three quarks in the baryon and a quark-antiquark-pair in the meson case. However, more complicated *exotic* states which are not covered by the

simple constituent quark model, are also predicted.

Since gluons are carriers of color themselves, they should be able to form a bound state with no valence quarks, called a *glueball*. The lowest state of that kind is predicted by lattice QCD to have quantum numbers  $J^{PC} = 0^{++}$  and a mass within a range of 1500 – 1800 MeV/c<sup>2</sup>.

*Hybrids* can be formed as a combination of a meson and an excited gluonic state ( $qg\bar{q}$ ). These states can be distinguished from meson states by quantum number combinations that are not allowed in simple quark-antiquark combinations of the three light quarks - QCD predictions expect states with  $J^{PC} = 0^{+-}, 1^{-+}, 2^{+-}, 3^{-+}$  at a mass of approximately 1400 – 1600 MeV/c<sup>2</sup>. Further exotic states like *tetraquarks* ( $qq\bar{q}\bar{q}$ ) and *pentaquarks* ( $qqqq\bar{q}$ ), also occupying exotic quantum numbers, have been proposed but not yet established [COM05b][COM10b].

In any of these cases, the surrounding energy region needs to be well-known in order to extract these exotic signals from the recorded spectrum. In addition, the signal can be observed in various decay channels, differing in particle multiplicities and charges. In COMPASS, charged exotic states are searched in *diffractive scattering*  $\pi^- p \rightarrow X^- p$  while neutral states arise via *central production*  $pp \rightarrow p_{fast} X^0 p_{slow}$ . The beam is adjusted depending on the physics process that is chosen to be recorded, and also kaon "impurities" of the negatively charged beam are used for analysis.

## Drell-Yan muon pair production

In the Drell-Yan reaction, a quark and an antiquark from beam and target annihilate and the resulting photon decays into two leptons. This process yields a possibility to investigate parton distribution functions of hadrons without the involvement of fragmentation functions.

### 2.1.2 Physics with muon beam

#### Longitudinal Spin Structure

In inclusive deeply inelastic scattering (DIS) of a polarized muon beam off a longitudinally polarized target,  $\vec{\mu} \vec{N} \rightarrow \mu' X$ , the helicity structure function  $g_1^d(x)$ , where  $x$  is the Bjorken scaling variable, can be measured as well as its asymmetry  $A_1^d$  [COM05a] [COM07d]. Having measured  $g_1^d$  with high precision, the quark contribution to the nucleon spin can be deduced to be  $\Delta\Sigma = 0.33 \pm 0.03(\text{stat}) \pm 0.05(\text{sys})$  [COM07b]. From the same measurements, polarized valence quark distributions [COM08] and flavour-dependent helicity distributions [COM09b] can be calculated.

### Transverse Spin Structure

By measuring semi-inclusive DIS on a transversely polarized target, one has access to the transverse spin structure, which is hidden in other measurements.

The Collins and Sivers asymmetries that can be measured in semi-inclusive DIS on a transversely polarized target when detecting the hadron with the highest momentum have been measured by COMPASS on a deuterium target for outgoing pions and kaons. The results are small, and compatible with zero within the error margins [COM07c][COM09a]. The measurement on polarized hydrogen has been performed, but no results have been released yet.

### Gluon Polarization

The spin of a baryon is constituted like

$$(2.1) \quad \frac{1}{2} = \Delta\Sigma + \Delta G + L_q + L_g,$$

with  $\Delta\Sigma$  the sum of all quark spins,  $\Delta G$  the gluon spin contribution and  $L_{q,g}$  the intrinsic angular momentum of the baryon. While the quark-parton model expected the contribution from quark spins to be around 60% of the total spin, it was measured by the precursor of COMPASS, the EMC (European Muon Collaboration) [Col89] and confirmed by other experiments to be only about 25%.

Expecting the orbital angular momentum to be zero for the lightest hadrons, there is only the gluon polarisation left to contribute. Since gluons cannot be observed directly via photons, a higher-order process, including production of a quark-antiquark pair via *photon-gluon-fusion* is necessary. A very promising channel for this topic is the *open charm*, where the produced quark-pair is a  $c\bar{c}$ , fragmenting into D mesons.

Another way of determining the gluon spin contribution is to look at events that contain hadrons with high transverse momentum which can best be analysed in events with high transverse momentum  $p_t$  [COM06].

### $\Lambda$ and $\bar{\Lambda}$ Polarization

In the simplest case of polarized  $\Lambda$  production, where an unpolarized muon beam scatters off a unpolarized target, polarization is related to the hadronization process and is not fully understood. However, at COMPASS with a polarized target and beam, conditions are better defined and one can try to study the parton spin-transfer to hyperons. Due to the parity-violating weak decay of the  $\Lambda$ , the polarization can be directly extracted from the angular decay spectrum.

## Deeply virtual Compton scattering (DVCS) and deeply virtual meson production (DVMP)

In DVCS measurements, a high-energetic virtual, but almost on mass-shell photon scatters off a parton, however leaves the hadron intact. Due to the small momentum transfer, the virtual photon is turned into a real one. This gives access to the *generalized parton distributions* (GPDs), that are a combination of parton distributions and elastic form factors of a hadron. They will give information about angular orbital momentum of partons.

This measurement requires a variety of measurements of hard exclusive processes, i.e. with all outgoing particles known. DVMP offers a complementary measurement that covers different linear combinations of GPDs.

## 2.2 Spectrometer setup

### 2.2.1 The M2 beam line

The CERN SPS accelerator delivers the primary beam for the beam line of COMPASS. The protons with an energy of 450 GeV hit the primary target "T6" which typically consists of a block of beryllium of a length up to 500 mm. The produced secondary particles - mostly hadrons - follow the 600 m long decay line. Bending magnets bring the beam from the underground accelerator and primary target up to the experimental area. Whether it is tertiary muons or electrons, or secondary hadrons that follow the beam line, can be determined by placing hadron absorbers in the path of the beam. The beam charge and energy can be chosen via polarity and field strength of the bending magnets and a number of collimators.

### Muon beam

For muon beam, the decay channels of pions and hadrons into muons are used. After a 600 m long decay section, the hadrons are stopped by a 9.9 m long beryllium target. The beam is additionally purified by placing a thick concrete absorber directly before the beam's entrance into the COMPASS experimental area. Since the majority of the muons is produced in charged pion decay, they are naturally polarized in their center of mass system. With a defined pion energy, by selecting a certain muon energy one can select the direction of the decay and thus its helicity. This way, a polarized muon beam of selectable polarity can be produced. The beam energy can be selected in a range from 60 to 190 GeV and typically has a beam spot size of about  $7 \times 8 \text{ mm}^2$  RMS. The flux is limited by the radioprotection guidelines and can go up to  $2 \cdot 10^8$  muons per SPS cycle<sup>3</sup>.

<sup>3</sup>The COMPASS beam is divided into *spills*, following the structure of the SPS cycle with a length of 45s, of which 9.7s are *on-spill* for COMPASS, i.e. beam particles are delivered to the experiment

### Hadron beam

The negatively charged hadron beam is composed mostly of pions with a fraction of kaons and muons and a small part of antiprotons and electrons (if a beam with positive charge is chosen, there are mainly protons). The beam energy is adjustable in a range from 40 to 280 GeV and the maximum allowed intensity is  $10^8$  particles per SPS cycle. The beam spot can be tuned down to an RMS of  $1.1 \times 1.5 \text{ mm}^2$ .

### Electron beam

The tertiary electron beam mainly serves for calibration purposes of the electromagnetic calorimeters. Low energy particles (below 100 GeV) are selected and focused on a converter target. Energies in a range from 10 to 60 GeV can be adjusted and typical beam spot sizes lie around 8 mm RMS.

### 2.2.2 Spectrometer regions

The spectrometer can be divided along the beam direction into three basic regions: the region upstream of the target, the large angle spectrometer (LAS) and the small angle spectrometer (SAS), both introduced by a dipole bending magnet. All information in this section, if not referenced differently, is taken from [COM07a].

The region upstream of the target is equipped with several scintillating fibres and silicon detectors for definition of the incoming beam particle. In addition, veto detectors are used to reject events that originate from beam halo particles and thus do not hit the target.

The large angle spectrometer is close to the target and covers particles in the lower energy range of 1 – 20 GeV. Sandwiched by several tracking detectors is the SM1 dipole magnet with a bending field integral of 1 Tm. Following SM1 the Ring Imaging Cherenkov detector (RICH) can identify charged particles with momenta of up to 60 GeV. Downstream of that there is the electromagnetic calorimeter ECAL1 and the hadron calorimeter HCAL1, both with a hole in the center for the beam and SAS particles to pass through. The LAS is concluded by the muon filter MW1 to identify muons.

The SAS, tracking particles with energies above 5 GeV and with scattering angles  $< 30 \text{ mrad}$  from the beam direction, begins right behind the LAS with the 4 m long, 4.4 Tm field integral SM2 that is again surrounded by tracking detectors. Following, there are the ECAL2 to determine electron and photon energies and HCAL2 for hadrons' energies. The SAS is again concluded by muon filter MW2.

## 2.2.3 Detector components

### 2.2.3.1 Tracking Detectors

Several different types of tracking detectors are used in COMPASS to account for different requirements depending on the particles and acceptance region they are supposed to measure. Especially detectors near and in the beam require a radiation-hard design as well as good spatial and time resolution. At the same time, the material budget that comes along with the detectors needs to be minimised to reduce the probability of scattering or other interactions inside the detector material.

Very small area trackers (VSAT) are used for precise definition of beam particles and particles with a small scattering angle. Due to the high count rate of several  $10^6/s$  for the hadron and  $10^8/s$  for the muon case, hits need to be associated to a track by using their time information. The Scintillating Fibre (SciFi, FI) detectors provide excellent time resolution in the order of 400 ps. They are placed at different places near the beam along the spectrometer. Depending on the beam focus at the given position, their active area varies from  $5.3 \times 5.3 \text{ cm}^2$  to  $12 \times 12 \text{ cm}^2$ . Silicon Microstrip detectors are used due to their excellent spatial resolution in the order of  $10 \mu\text{m}$  as a telescope for beam definition and, if the physics program requires it, vertex detection. They have a double sided readout to reduce the material budget and are designed to withstand high irradiation levels. A detailed description of the silicon detectors and their properties is given in the chapters 3 and 4.

Small area trackers (SAT) are useful for detecting particles at small distances from the beam axis. There are two established types of gaseous detectors at COMPASS, the three Micromegas (**micromesh gaseous structure**) with an area of  $40 \times 40 \text{ cm}^2$  between target and SM1 and 22 GEMs (**Gas Electron multiplier**) with an area of  $31 \times 31 \text{ cm}^2$  further downstream along the complete spectrometer. Both detector types have good spatial and time resolution in the order of  $70 \mu\text{m}$  and up to 8 ns. The second generation of GEMs, with up to five detectors along the spectrometer, has a pixelized readout in its center where the beam passes.

Large area trackers (LAT) are there to cover the large angle acceptance of the spectrometer. Three drift chamber detectors (DCs) are placed around the SM1 with an area of  $1.8 \times 1.8 \text{ m}^2$  and a 30 cm central dead zone. Six larger Drift chambers are installed downstream of the SM2, with an area of  $5.2 \times 2.6 \text{ m}^2$  and a 50 cm dead zone. In the LAS stage, there are the Multiwire proportional chambers (MWPCs), while in the SAS, there are the straw tube chambers (Straws) with a  $3.2 \times 3.2 \text{ m}^2$  area and a  $10 \times 20 \text{ cm}$  dead zone.

### 2.2.3.2 Particle Identification

Muons can be identified by their ability to penetrate material deeper than any other type of particle. The two muon walls both work with that property: they consist of an absorber material enclosed by two tracker detectors. The absorber needs to be thick enough to stop

all hadrons - a guidance value of 30 radiation lengths is usually chosen - so if a track is recorded both in front and behind, the particle is a muon. The LAS muon filter consists of an iron absorber with a 60 cm diameter, with moderate-resolution gaseous wire detectors (MW1). For the SAS, the absorber is a wall of 2.4 m of concrete, the tracking detectors are constituted by the trackers downstream from SM2, and an additional two MW2 stations and three MWPCs.

The Ring Imaging Čerenkov detector (RICH) can distinguish between types of hadrons making use of the fact that Čerenkov light is emitted at a known angle. It depends on the refractive index of the surrounding medium, the energy and the mass of a particle. In a gas vessel with a  $80\text{ m}^3$  volume, filled with the radiator gas  $\text{C}_4\text{F}_{10}$ , the emitted photons are reflected by two spherical mirror surfaces to the CsI photon detectors, which convert them into electrons that are subsequently detected by MWPCs. The RICH covers a momentum range of about 5 – 60 GeV and the complete angular acceptance of the LAS, with the exception of a 10 cm diameter beam hole in its center.

### 2.2.3.3 Calorimetry

The hadron calorimeters, positioned between the electromagnetic calorimeter and the muon filter of both spectrometer stages, consist of alternating layers of hadron absorber (iron, steel), where hadronic interaction is induced and a hadronic shower is produced, and scintillator material, where the absorbed energy is transformed into photons that can then be detected by photomultiplier tubes (PMTs). HCAL1 consists of 480 modules, each  $14.2 \times 14.6\text{ cm}^2$  wide with 40 layers of 20 mm iron absorber and 5 mm scintillator. There is a  $8 \times 4$  cells wide beam hole in the center that allows unscattered beam particles to go through. HCAL2 has 216 cells ( $22 \times 10$  with a  $2 \times 2$  beam hole) with a width of  $20 \times 20\text{ cm}^2$  and 36 layers of a 25 mm steel absorber and 5 mm of scintillator material.

The electromagnetic calorimeters are placed right in front of the HCALs. They are constituted of lead glass cells with a high refractive index. Whenever an energetic charged particle or photon hits the material, an electromagnetic shower of  $e^+e^-$ -pairs develops that radiate Čerenkov photons, which can again be detected by PMTs at the end of each cell. ECAL1 is built from 1508 cells of 3 different sizes. ECAL2 has  $64 \times 48$  cells, each  $38 \times 38 \times 450\text{ mm}$  big, with a variable beam hole with a size dependent on the beam parameters.

## 2.2.4 Specifics for hadron beam

**Targets:** In target thickness, a trade-off between high statistics and multiple scattering needs to be made. The target design and material differ with different aims of physics. For the 2004 hadron run, different targets materials from medium to high atomic numbers values were tested. In 2008, a proton target in form of a liquid hydrogen tank was used. For the 2009 Primakoff test run, a target with a sequence of thin foils of nickel and wolfram was created, for diffractive data a sequenced lead foil target was used.

**Recoil proton detector:** Since 2008, the target is surrounded by a cylindrical detector, the RPD. It consists of two layers of scintillator, which is enough to identify low momentum recoil protons. The momentum can be determined with a time-of-flight (TOF) measurement. It can also be used as a veto for physics that require very low momentum transfer to the target, i.e. Primakoff data.

**Vertex reconstruction:** Starting 2008, very close after the target, still positioned inside the RPD, is the conical cryostat with two silicon stations that serve as a vertex detector. In 2004, three separate stations were used.

**Beam particle identification:** As the beam contains a small fraction of about 4.5 % kaons, it is necessary to distinguish the beam particles. The two CEDARs (Čerenkov Differential counters with Achromatic Ring focus) can set the threshold for Čerenkov radiation by adjusting their gas pressure. When correctly set, the threshold lies between pion and kaon mass (for a given energy).

**Trigger:** The minimum bias hadronic trigger consists of a beam trigger which requires coincident hits in two scintillators upstream from the target, and vetos for particles too far from the beam axis to hit the target and scattered particles with an angle that exceeds the spectrometer acceptance, as well as a veto for unscattered particles (the "beam killer"). Primakoff events produce high-energetic photons, so the Primakoff trigger is defined by the minimum bias trigger plus a cluster with an energy greater than 60(40) GeV in the ECAL2.

Diffraction events are characterised by a larger number of outgoing particles. In order to be sensitive also to the production of neutral pions, which are not detected in the multiplicity counter, the DT0 trigger requires a proton in the RPD in coincidence with the minimum bias trigger. Since this trigger is only sensitive to high momentum transfer, the additional all-t trigger that was installed for some time in 2009 is a coincidence of minimum bias and high rates ( $> 2$ ) in the multiplicity counter in the low momentum transfer case.

**Others:** The beam hole in the ECAL2 is  $2 \times 2$  cells wide, corresponding to the size of the beam at the ECAL2 coordinates. Scintillating fibres along the beam are removed in order to reduce material budget. For the same purpose, during Primakoff data taking the RICH is filled with nitrogen, which has a lower density than the radiator gas  $C_4F_{10}$ .

**Drell-Yan plans:** The feasibility of Drell-Yan studies was tested in short periods in the years 2007, 2008 and 2009 and is discussed in the proposal for COMPASS-II [COM10a]. Data taking will require a higher beam intensity than currently permitted by radiation protection (cf. section 2.2.1) and the corresponding safety measures will have to be taken. Part of that will be an absorber that "kills" the hadron beam a short distance after the target.

### 2.2.5 Specifics for muon beam

**Polarized target:** In COMPASS muon physics, a polarized muon beam interacts with a polarized target. The polarization of the deuterated lithium ( ${}^6\text{LiD}$ ) target is achieved via *Dynamic Nucleon Polarization*: Paramagnetic centers (free electrons on impurities) are polarised and can then give their polarization to the nucleus. The polarization is provided by a superconducting solenoid with a field of 2.5 T. In order to measure asymmetries, there are either two or three cells that are polarized in opposite direction.

**Beam momentum stations:** The momentum of the muon beam has a spread of about 5%. To define the momentum, around one bending dipole magnet along the beam lines, there are several scintillators (3 before, 3 after the magnet) that form the beam momentum station (BMS). They observe the bend of the track and can thus determine the momentum with a precision of 1%

**Trigger:** The minimum bias trigger for the muon programme is set for inelastic scattering, i.e. scattered muons. It is complimented by vetos that guarantee the beam particle hit the target.

**Others:** The beam hole in ECAL2 is expanded to  $10 \times 10$  cells since the muon beam is wider than the hadron beam. The RICH is always filled with the usual radiator gas  $\text{C}_4\text{F}_{10}$  in order to be able to distinguish between outgoing pions, kaons and protons.

**DVCS plans:** The prospects of DVCS and DVMP measurements are discussed in the proposal paper for COMPASS-II [COM10a]. While trigger equipment is already available from muon programme and the recoil proton detector can be used to grant exclusivity, an upgrade of electromagnetic calorimetry will be desirable. An essential step in this direction was the construction of an ECAL0 prototype module in 2010. The possibility of constructing a new RPD that extends further along the beam axis, in order to have a larger angular coverage of recoiling protons, is in discussion as well as the usage of a polarized target.

## 2.3 Readout chain and analysis tools

The following sections give a brief overview on how the data collected by COMPASS is managed and on how raw data becomes a physics "event" with particle tracks and their associated vertices.

### 2.3.1 Data acquisition

When a trigger occurs, a readout signal is sent to all detectors' frontend electronics. Signals from all channels above a detector-specific threshold are sent to the *readout buffers* (ROB) and from there to the *eventbuilders* (EB, EVB), which collect data from all detectors and store them as a complete *event*. Events are stored in chunks of up to 1 GB size and are

written on tape to CASTOR, the CERN Advanced STORage manager [CAS]. The COMPASS Data Acquisition (DAQ) needs to be able to deal with trigger rates up to 300 000 per SPS cycle for muon data (in 2010), and up to 500 000 events for hadron data (2009). Average event sizes are approximately 27 kB in the hadron and 44 kB in the muon case.

### 2.3.2 Cinderella - The online filter

The online filter cinderella [Nag05] was written in order to reduce the amounts of data COMPASS records (several hundred terabyte per year). Cinderella acts as a software trigger, preselecting events that will be useful in physics analysis. When filtering is active, only events with a sufficient number of hits in the beam telescope (beam momentum station, scintillating fibres, silicons) are stored, others are rejected. In 2004, for muon beam about 23% of all triggered events were rejected, while for hadron data taking the triggers were reduced by 46% for the diffractive trigger by cutting on the number of hits in the silicon vertex detector. Since the filter is very sensitive to detector performance, and thus high-maintenance, in the years after 2004 it was mainly used for marking events, "bad" events were not rejected.

### 2.3.3 The ROOT analysis framework

ROOT is an object-oriented framework that was developed in 1994 at CERN as a successor to the Fortran-based PAW [ROO]. It is equipped especially to suit the needs of high energy physicists, designed to cope with huge amount of data. By storing data in specially designed TTrees, disk space can be minimized. At COMPASS, ROOT is used by the online monitor COOOL and for advanced analysis. For this purpose, Coral links the event reconstruction to ROOT. Within this thesis, ROOT is used for histogramming, data display and fitting purposes.

### 2.3.4 Online monitoring with COOOL

COOOL is a ROOT-based tool which is used to examine data live during data taking. It creates histograms and TTrees that are useful to check on detector performance. Data can be examined both online (streamed directly from an eventbuilder) or offline (reading the stored raw data). A rudimentary track fitting method is available which is sufficient for detector studies that require reconstructed straight tracks.

### 2.3.5 COMGEANT spectrometer simulation

COMGEANT is based on the high energy physics simulation framework GEANT 3.21 and was created to simulate the behaviour of particles in the COMPASS spectrometer [COM]. Generators are used to create photon, lepton or hadron interactions. *geometry*

*files* can be created, which denote the positions of detectors and are used in later data processing by Coral. In the *material maps* the material budget of the complete spectrometer is stored in detail. In the material, interactions are produced using random distributions, in accordance with their statistical nature. The trajectory of particles is propagated through the spectrometer and their hits in detectors are stored with position and deposited energy.

### 2.3.6 Event reconstruction with Coral

The COMPASS Reconstruction and AnaLysis project "Coral" is used to build up tracks and vertices from the hits in detectors that are stored by the DAQ or Monte Carlo Simulations. In order to have the full information on the event, the following steps have to be taken:

- **Decoding:** From the raw data, informations ("digits") for single wires/cells/pads that delivered a signal are extracted. For Monte Carlo data, these informations are not yet available, instead they are generated ("digitisation") from the information on position and energy deposition of a track crossing the detectors.
- **Clustering:** From the digits of neighbouring channels, the information is grouped into *clusters*.
- **Tracking:** The information available from the single detectors is used to reconstruct particle trajectories. This is done in the following steps:
  - The spectrometer is split into several *zones* along the beam axis for purposes of pattern recognition. In every zone, single track segments (or track projections) are reconstructed in detector projections at first.
  - By association of different projections (two at least), track segments are combined to full trajectories confined to a single zone.
  - In the bridging part, tracks from different zones are connected to one track through the complete spectrometer, including the bend that originates from the spectrometer magnets.
  - The track fitting method determines all parameters and corresponding errors of the charged particle trajectories using the Kalman filter technique. The track time is calculated, using the time information of all detector projections.
- **Calorimeter reconstruction:** With the knowledge about shower profiles, an energy deposit is estimated for every cell. Then, cluster energy and position are determined with a fit using the information from multiple cells.

- **RICH reconstruction:** In the gas mixture of the RICH, high-energetic particles radiate Čerenkov photons at an angle that is given by the particle mass and energy. The probabilities of the particle to be a proton, kaon or muon are calculated.
- **Vertexing:** In order for the event to contain complete information, the position of interaction and decay vertices has to be found. Coral first determines the point of closest approach for all tracks, and if the distance goes below a defined threshold, the point is selected as a vertex.

All reconstructed information is stored into ROOT `TTrees`, called *mini Data Summary Trees (mDST)*. They are the basis for all following physics analysis and the compression factor compared to raw data is about a factor 100 for muon data and a factor of 4 in hadron data, which still contains a significant part of raw information. When given the corresponding option string, Coral also stores informations about single hits (MegaDST) or all digits (GigaDST) for a specified detector type or projection.

In order for mDST mass production to start, all calibration parameters need to be fixed first. In *time calibration*, the time reconstruction is modified to be in line with the trigger times. For *alignment*, the multidimensional space of detector positions, angles and channel pitches is adjusted to minimise the errors of tracks. This is a very delicate operation, since there are many local minima and there are several thousand parameters to be adjusted. The determined parameters are written to a text file called the *alignment file* or *detectors.dat file*. During beam time, an alignment run is performed regularly, once with both spectrometer magnets on and off, with a defocused beam at low intensity. This way, the variety of tracks is wide enough to determine the alignment parameters.

### 2.3.7 PHAST - Data analysis

**PHysics Analysis Software Tools** is a toolkit for analysing COMPASS data at mDST level. In order to create mDSTs, PHAST needs to be linked to coral. It was developed to have quick direct access to all important information on physics data. A distinct user section allows to write an own *UserEvent* function, which is called for every event that is looped over. The output of PHAST can either be a ROOT file, containing histograms and/or `TTrees` one can work on within the ROOT framework, or a  *$\mu$ DST* file, which contains events or event parts that are specially filtered for the analysis that is supposed to be done with them.



## Chapter 3

# The COMPASS silicon microstrip detector

This chapter describes in detail the setup of the silicon microstrip detectors, their readout and their cooling system as is was operated in 2009 and 2010. An extensive description of the non-cryogenic setup is given in [Din11]

### 3.1 Working principle

In high energy particle physics, silicon strip detectors are often used for tracking due to their ability of achieving excellent spatial resolution. Usually, they are constituted by a 300 – 500  $\mu\text{m}$  thick layer of n-type silicon, lightly doped with electron donors (e.g. phosphor) and a thin layer (in the order of 1  $\mu\text{m}$ ) of p<sup>+</sup>-type silicon implants, doped with e.g. boron atoms as acceptors in a high concentration. These two layers constitute a p-n-junction, and thus a diode. In the border region, the charge carriers (holes in the p-layer, electrons in the n-bulk) recombine and as a result this border region is a practically carrier-free depletion zone.

Due to their different doping concentrations, this zone is strongly asymmetric and extends far into the n-bulk. When applying a voltage in reverse-bias direction, the zone becomes even larger, up to the point where the complete bulk is depleted. The behaviour of the wafer in this situation is capacitor-like: It draws no current. When a charged particle traverses the detector, it generates electron-hole-pairs along its trajectory, which drift towards the n- (electrons) and p-electrode (holes) of the applied voltage and generate a signal in the readout electronics. To be position-sensitive, the p- and n-electrodes are split up and arranged in a strip pattern, placed upon the bulk.[Pei92][Spi05][Leo94]

## 3.2 The COMPASS silicon detector setup

### 3.2.1 Requirements

In COMPASS, the silicon detectors are used for beam definition and, when using a hadron beam, for precision tracking and vertex reconstruction of the scattered particles. To cope with the high beam intensities in the order of magnitude of  $2 \cdot 10^8$  particles per spill, the detectors require a radiation-hard design and good time resolution in the order of one to a few nanoseconds to be able to separate particles. Especially for the vertex detector in hadron runs, an excellent angular resolution in the order of  $150 \mu\text{rad}$  is crucial for precise vertexing. A low material budget decreases the chances of multiple scattering and is therefore highly required.

### 3.2.2 Wafer design

The silicon wafer, optimised for high fluxes, was originally designed and developed for the HERA-B experiment [SP95] by the Semiconductor Laboratory (HLL) of the Max-Planck-Institutes in Munich and produced by SINTEF in Oslo (Norway) [Sin97]. Its double-sided readout is a feature that allows to reduce the material budget by a factor of two, taking into account only the wafers, not the station windows (cf section 3.2.5). It also results in a correlation of hit amplitudes on both sides that would not arise in usage of two detectors with single-sided readout, and that can be used in event reconstruction to improve results.

The wafer is  $300 \mu\text{m}$  thick and has an active area of  $7 \times 5 \text{ cm}^2$ . There are 1280 strips on the n-side and 1024 strips on the p-side, with a pitch of  $54.6 \mu\text{m}$  and  $51.7 \mu\text{m}$ , respectively. Strips on opposing sides are arranged perpendicularly, so a single detector module yields two-dimensional information on a crossing particle. The strips have a relative tilt of  $2.5^\circ$  to the geometry of the wafer, matching the requirements of the HERA-B experiment.

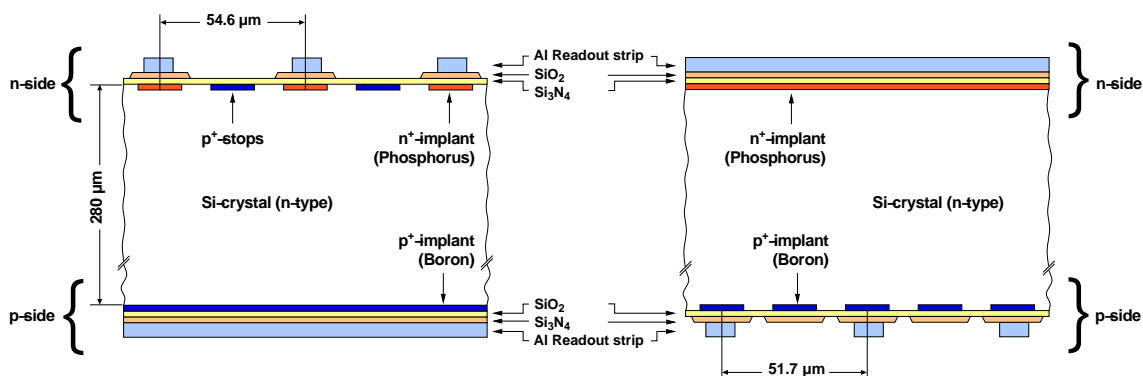


Figure 3.1: Cross section of the silicon wafer

The Wafers are designed to withstand a equivalent annual particle flux of up to  $3 \cdot 10^{14}$  minimum ionising particles per  $\text{cm}^2$  [Pug99]. As this rate is exceeded in the beam center, radiation damage is induced, leading to leakage current. That means readout via capacitive coupling is required. Thus, the aluminum readout strips are separated from the silicon bulk by layers of silicon dioxide and silicon nitride. There is a multi-guard-ring structure around the wafer that controls the drop of the bias voltage towards the potential of the undepleted substrate [Abt96]. The bias voltage is applied to the ring, and from there to the strips via  $1 \text{ M}\Omega$  polysilicon resistors.

In order to avoid shorts, on the n-side the strips are separated from each other via *p-stop* implants. On the other hand, on the p-side there are intermediate p-strips that increase spatial resolution by sharing their collected charge with both neighbouring strips via capacitive coupling.

### 3.2.3 Detector module

The silicon wafer is fixed with silicone glue between two L-shaped printed circuit boards (PCBs), called the *L-Boards*. They provide all necessary infrastructure near the wafer, like power connectors, connections for data transmission, temperature sensors, the frontend readout APV chips - 8 for the 1024 strips of the p-side and 10 for the 1280 strips on the n-side, 128 channels per chip - and the *pitch adapter* that matches the pitch of the strips on the wafer to the bond pads of the readout chips. Soldered along the edges of the boards is a capillary<sup>1</sup> bent in a sine-like shape (for cold operation), through which nitrogen (gaseous or liquid, depending on cooling operation, see sec. 3.3) flows to cool the wafer and APV chips.

### 3.2.4 Frontend electronics and readout chain

#### The frontend APV chips

The APV25 chip is an analog pipeline ASIC<sup>2</sup> that was originally designed for the CMS<sup>3</sup> experiment at the LHC<sup>4</sup>. Each of the 128 channels consists of a CR-RC-type shaping amplifier and a 192 sample analog pipeline. The signal generated by the charge carriers arriving from the strips is shaped and turned into a well-defined voltage signal. This signal is continuously sampled by the chip with a frequency synchronized to the TCS<sup>5</sup> reference clock with 38.88 MHz.

Of the 192 memory blocks on the analog pipeline, 160 act as a ring buffer that is used to account for the latency of the trigger. At the given readout frequency, signals can be

<sup>1</sup>Inner/outer diameter 1.3/1.6 mm, material: Cu/Ni alloy (Alloy 400)

<sup>2</sup>Application Specific Integrated Circuit

<sup>3</sup>Compact Muon Solenoid

<sup>4</sup>Large Hadron Collider

<sup>5</sup>Trigger Control System

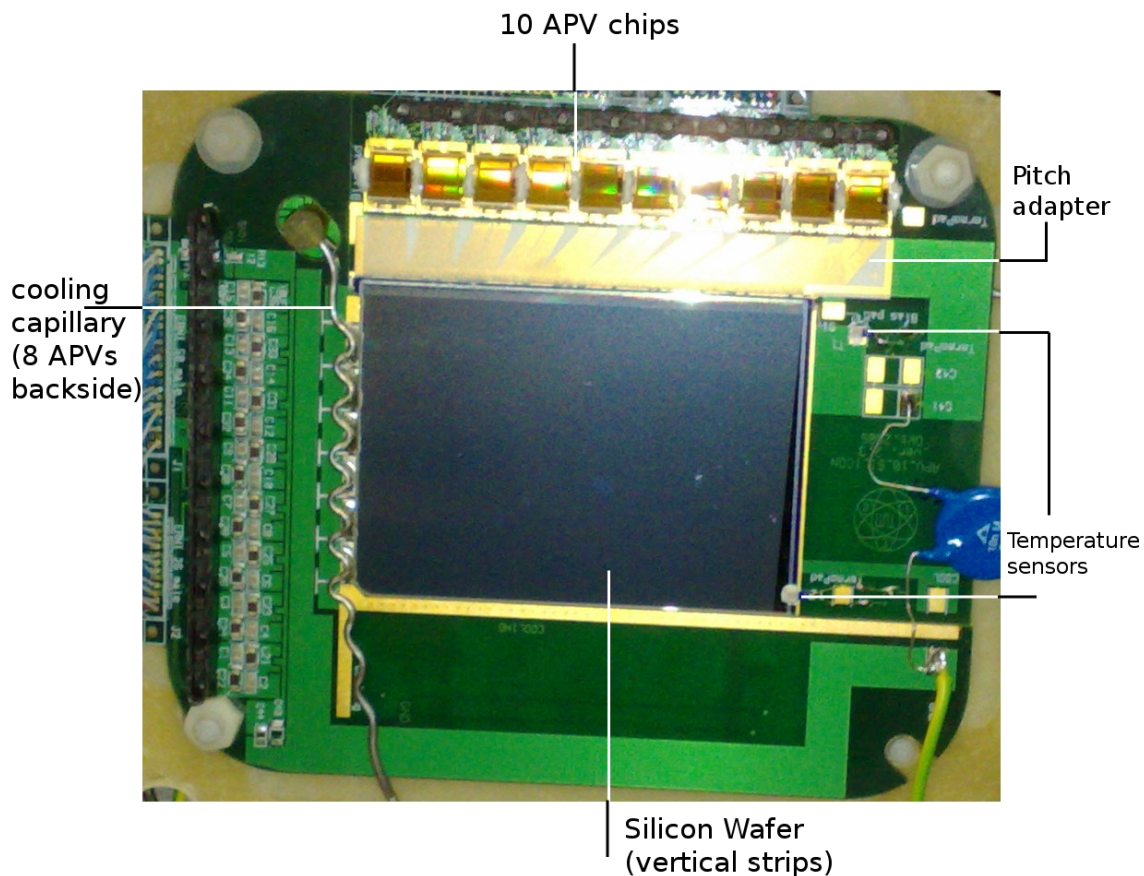


Figure 3.2: The silicon detector module

stored for up to  $8 \mu\text{s}$ . The trigger pointer of the ring buffer flags the pipeline column in case of an external trigger signal for readout. The according samples are then written to the remaining 32 memory cells of the pipeline that are organised as a FIFO<sup>6</sup>, and from there, are sent out, multiplexed on a single differential output line.

The chips are operated in *multi-mode*, that means that with one trigger signal, three consecutive samples from the ring buffer are assigned for readout. These three samples deliver precise time information that can be extracted on software level (cf. section 4.2). For more detailed information on the APV25, see [Jon].

<sup>6</sup>First-in-first-out, basic electronics concept

## Readout chain

The detector modules are connected via flat band cables to the *repeater cards*, which connect to the electric feedthrough from inside the station to the readout. They supply the APV chips with a low voltage of  $\pm 3.3$  V, amplify the delivered signal via a high speed operational amplifier and provide separate lines for temperature readout, clock and trigger input.

The signals are then sent to an ADC card (named SGADC) via another flat band cable, where they are digitised by 10 bit ADCs with a sampling rate of currently 20 MHz, an upgrade to 40 MHz firmware is planned. The main processing is going over two FPGAs<sup>7</sup>. Using a pedestal subtraction and zero suppression algorithm, the data rate is strongly reduced: The algorithm subtracts a (previously recorded) pedestal value, and the remainder is compared to the (also previously recorded) noise level of the strip, and if it is significantly higher (e.g. by a factor 3), it is assumed to be a signal and will be further processed. A "common mode correction" is applied for both the pedestals and the actual data, it corrects common fluctuations in signal output of all 128 strips hosted by one APV chip. This makes it possible to correct for fluctuations e.g. in power supply for the APVs.

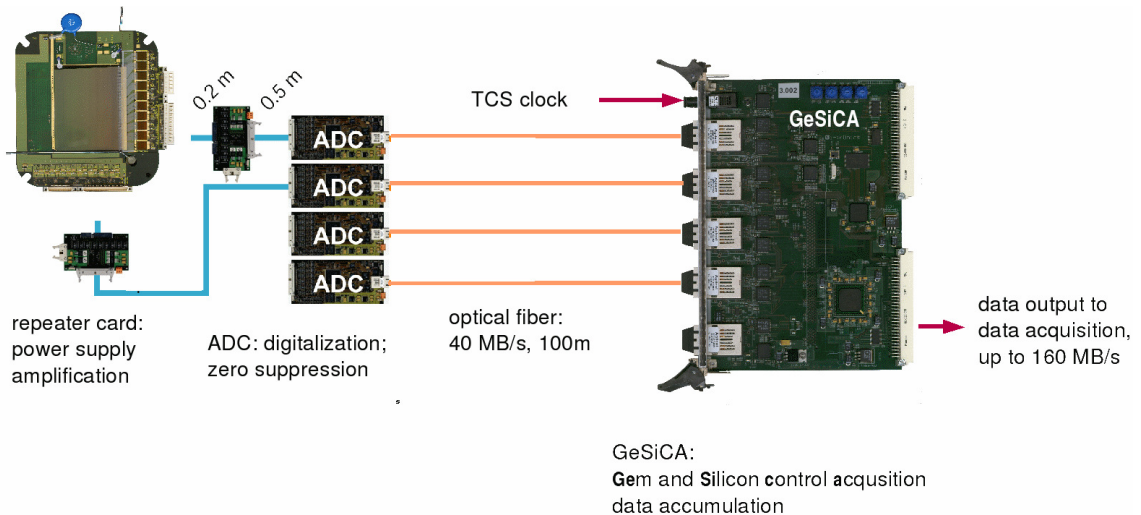


**Figure 3.3:** Readout chain, from [Din11]

The pedestals and common mode noise levels are recorded in a dedicated *pedestal run*, where the ADCs are set to *latch all* mode, which means no pedestal subtraction takes place and all strips are read out. The remaining signals are formatted into 4 Byte words and, via an optical fiber of 50 m length, sent to the **GEM and Silicon Control Application (GeSiCA)**. This card is electrically decoupled from the ADCs, repeater cards and detector modules, which is necessary since it receives input from up to 4 detector planes, where a relative voltage (the bias voltage) is applied to two of them, respectively.

<sup>7</sup>Field Programmable Gate Array

The GeSiCA module distributes the TCS reference clock, trigger and reset signals to the frontend cards and multiplexes the streams from up to four ADC cards into one stream, which is sent to an optical link and from there into the data acquisition system.

#### 3.2.5 The detector stations

The detector modules have unique names like SI1.12, SI1.13, SI2.01, where the first number indicates the production (1 or 2), while the second number is a running index<sup>8</sup>. One complete station is referred to as SI0X (replacing X with a number), a module inside a station as e.g. SI02UV, and a single plane like SI02U or SI02U1\_\_(the technical board name, "TBName") for analysis purposes.

#### Upstream stations

Two detector modules, corresponding to four readout planes, are grouped into one detector station. They are mounted onto a frame of glass reinforced plastic (Stesalit), in a fashion that one module's strips have rotation angles with respect to the COMPASS main coordinate system of 0° and 90° (planes X and Y), while the other module is inserted reversely and tilted by 5° so its rotation angles are 5° and -85° (U and V). Along the Z-axis, the order of the planes is U, V, Y, X.

The cryostat was designed with the goal of cooling the modules with liquid nitrogen (cf. section 3.3), and is thus capable to sustain a vacuum. It provides connections for vacuum equipment (pump, gauge) on the bottom, for electric feedthrough to the repeater cards on the sides and top, as well as an inlet for liquid nitrogen on the top and three outlets on one side. The feedthroughs to the repeater cards are accomplished via standard commercial vacuum-tight 50-pin-feedthroughs.

On the front and back of the stations there are special beam windows mounted, designed for low mass density, minimizing the material budget in the beam line. The challenge of designing a vacuum-proof window with minimal mass density was solved with a aluminized mylar foil facing outside, which is supported by a carbon-fiber mesh on the inside.

#### The conical cryostat

The conical cryostat (CC) was designed to host four detector modules (i.e. an equivalent of two stations), to be operated as a vertex detector, a very short way downstream of the target during hadron runs. It is mounted into the downstream end of the recoil proton detector (RPD) barrel. All connections (vacuum, electronics, cryogenics) are on the downstream side, and the cryogenic equipment is placed in a separate box (the "phase

---

<sup>8</sup>Before the second production of modules, the convention was of the form SIL10, SIL11 etc.

separator box") outside the RPD. This alle serves the purpose of having a minimal material budget to minimize the probability of scattering particles that were produced (or scattered) in the target.

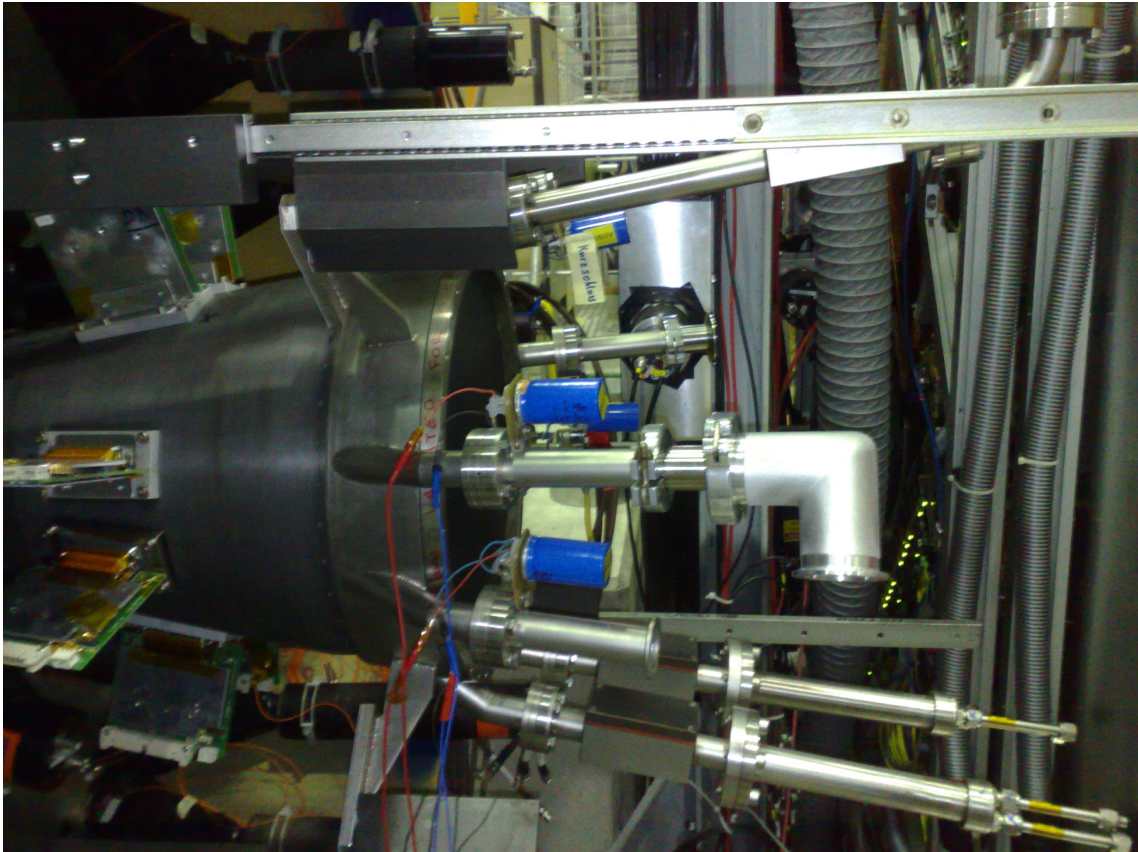


**Figure 3.4:** The CC during its dismount in november 2009

### 3.3 Cold detectors

Before 2009, the detectors were usually cooled by flushing the detector station with gaseous nitrogen. At a flow of about 300 l/h (at atmospheric pressure) per station, the operation temperature with powered APVs was around 55° C. In 2009, the COMPASS silicon detectors were for the first time constantly operated cryogenically at a temperature of 200 K. This section explains the motivation for cold operation and describes the cooling system. A more detailed description can be found in [Gra11].

#### 3.3.1 Purpose and principle

In the COMPASS-II upgrade [COM10a], the beam will contain up to  $10^8$  hadrons per spill (e.g. for Drell-Yan measurements), which is almost two orders of magnitude more than the current hadron beam. Thus, the detector will be strongly irradiated and take damage. The intention of cryogenic operation is to make use of the effect of irradiated silicon detectors, which causes a partial recovery of the charge collection efficiency [Pal98]. It has been experimentally determined that this effect reaches a maximum in efficiency at a temperature of 130K, however this temperature may bring some problems for the current detector design, as different temperature expansion coefficients of the silicon wafer and the L-boards will lead to mechanical stress that could result in damage to the wafer.

Another advantage of the cryogenic design is a more stable operation of the readout: The temperature can be kept stable with a fluctuation of about  $1^\circ\text{C}$ , while at non-cryogenic operation, a stronger thermal connection to the environment existed and the temperature depended strongly on external conditions beyond any control. With a more stable detector station, data quality becomes more stable automatically. The lower temperatures of the APV chips also have an influence on the readout, the resulting differences will be discussed in chapter 5

#### 3.3.2 Cryogenics

All detector stations are provided with liquid nitrogen from the "valve box", which is itself supplied from the COMPASS central dewar. The valve box is located next to the upstream stations on a concrete platform in front of the target. Via a cryogenic transfer line, the nitrogen flows to the inlets and into the phase separator of each station. From the phase separator, the liquid flows through the cooling capillaries, soldered to the L-board edges, and cools both the wafer and the APV chips. Afterwards, the now gaseous nitrogen goes through the outlets through a controlled flow meter and is released outside the experimental hall. By regulating the gas flow through the outlet, the temperature can be regulated. An additional controlled outlet regulates the pressure in the phase separator.

The upstream stations were found to accumulate condensed water upon the beam windows due to their low temperature in early 2009. This constituted a problem in the form of additional, uncontrollable material budget. The problem was solved by applying a thin plastic film over the windows and flushing the gap between foil and window with (gaseous) nitrogen.

### 3.4 Outlook

In parallel to this thesis, the foundation was laid for an upgrade of the existing detectors ([Bic11]):

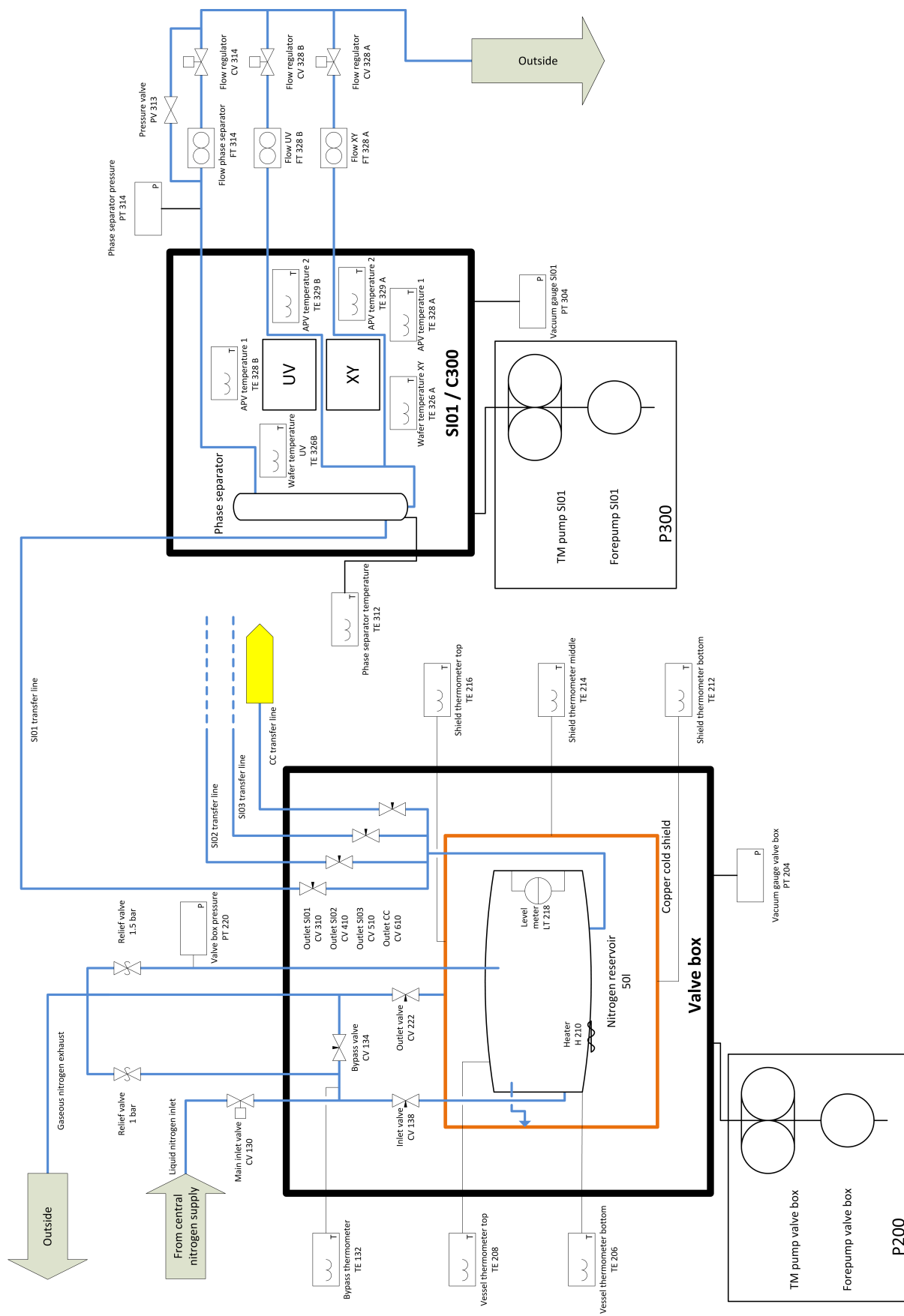


Figure 3.5: Schematics of the cooling system: valve box and upstream station, from [Bic11]

### 3 THE COMPASS SILICON MICROSTRIP DETECTOR

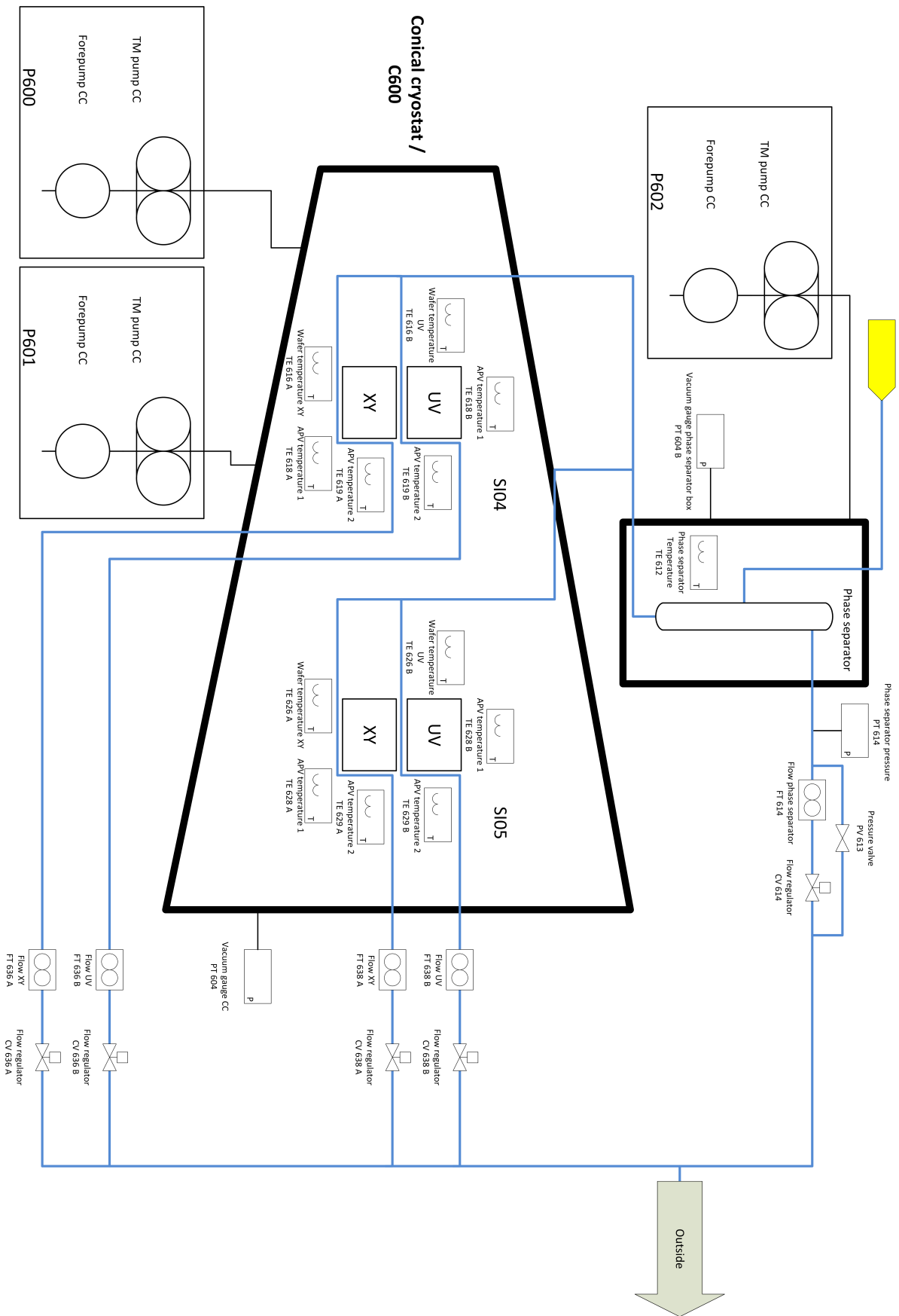


Figure 3.6: Schematics of the cooling system: conical cryostat, from [Bic11]

- The phase separator was re-designed to be more efficient.
- The detector module and support structure was redesigned to cope with different expansion coefficients in a better way.
- New cooling concepts were investigated to improve detector handling and reliability.
- There are plans for acquiring new sensors.

The main goal of this effort is to operate the detector modules reliably at 130 K. At the same time, various small problems that became apparent during operation, are sought to be solved.



## Chapter 4

# Data reconstruction for the silicon detectors

This chapter describes the way from a particle crossing the detector and exciting electron-hole pairs up to the point where a full cluster with position and time information is stored for the tracking method of the reconstruction software to make use of it. The results of this process, distinguishing between cryogenic and non-cryogenic operation of the detectors, will be shown in chapter 5.

### 4.1 Detector signal

When a charged particle crosses the detector, it produces electron-hole pairs in a cylindrical volume around the track. Per  $\mu\text{m}$ , a minimum ionising particle excites about 80 pairs of electrons and holes [Spi05]. The charge carriers drift, due to the applied bias voltage, to opposing sides of the detector. The charge collection time is about 10 ns for electrons and 25 ns for holes in a fully depleted silicon wafer with a thickness of  $300\ \mu\text{m}$  (cf. [PDG10]). The drift of charge carriers induces a current in the readout strips. Both types of charge carriers contribute on either side of the readout. Due to their different drift times, the major contribution early in the signal is caused by electrons, while the late part is constituted by holes only.

### 4.2 Time reconstruction

The APV chips (cf. sect. 3.2.4) are operated in *multi-mode*, that means for each trigger signal, three consecutive samples of the amplitudes are flagged for readout and sent to the ADC, where the pedestals subtraction and zero suppression algorithm is applied [Gru01]. Only for channels where at least one of the remainders of the samples exceeds the noise

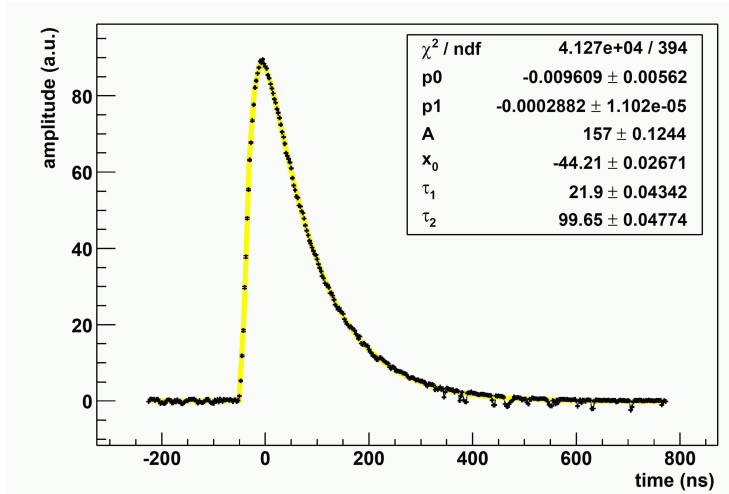


**Figure 4.1:** Response of the APV shaping circuit to a  $\delta$ -like input, from [Wie04]

level, the signal is processed to the GeSiCa and from there into the DAQ. The samples have a time difference corresponding to the TCS clock frequency

$$a_0 = A(t_{\text{Trigger}} - 2\Delta), \quad a_1 = A(t_{\text{Trigger}} - \Delta), \quad a_2 = A(t_{\text{Trigger}}),$$

where  $\Delta = 25.7$  ns.

In this thesis, when referring to the *amplitude* of a strip or cluster,  $a_2$  (or in the case of a cluster, the sums of  $a_2$ s) is meant.

It is convenient to introduce the TCS phase in order to define the trigger time with respect to the TCS clock:

$$(4.1) \quad t_{\text{TCS phase}} = t_{\text{TCS clock}} - t_{\text{trigger}}$$

While the amplitudes a particle causes differ widely, the shape of the signal remains the same and depends mainly on the frontend chips. In other words, the signal can, within the desired precision limits, be factorized as  $A(t) = A_0 \cdot r(t - t_0)$ , with  $r(t)$  being universally valid for all hits in one detector plane. Thus, by taking the ratios of the samples

$$(4.2) \quad r_0 = \frac{a_0}{a_2} \quad \text{and} \quad r_1 = \frac{a_1}{a_2},$$

the time-independent parameter  $A_0$  cancels out and the ratio, which has a fixed relation to the TCS phase, remains. This relation can be deduced completely from experimental data without making use of a model.

**Latency adjustment:** The latency defines the position in the APV ring buffer, where samples are marked for readout upon a trigger signal, and therefore is set in units of clock cycles. At the beginning of a beam time, it needs to be adjusted in a way that the rising edge of the signal corresponding to the event that caused the trigger is read out. Typical latency values are 75 in 2009 and earlier, and 78 in 2010. The values are defined by the time the trigger signal takes from generation to reaching the detector's readout electronics. The discrepancy between 2009 and 2010 arises from a migration of the trigger time by 78 ns via delay cables (cf. [Log] comment #34716) One latency setting covers a full TCS clock cycle, i.e. a 25.8 ns time window where times need to be reconstructed. Settings of half and quarter clock cycles - where the samples are recorded out-of-sync with the TCS clock - are possible to reach a better signal region.

**Latency scan:** The evolution of the ratios  $r_0$  and  $r_1$  with respect to the TCS phase can be seen in fig. 4.2. Within the marks is the shape in case of an optimal latency setting - with the first sample on the rising edge (corresponding to  $r_0 < 1$ ) and the second near the maximum ( $r_1 \approx 1$ ) of the signal. The figure also includes data from other latency settings, with a larger latency at lower values of the TCS phase the ratios go towards zero: the last sample ( $a_2$ ) lies on the rising edge, while the first two samples are taken too early, thus they are zero and so are the ratios. On the other hand, when choosing a too small latency, the ratios approximate a constant value: all samples are on the falling edge of the signal. Due to the exponential decay in this region the ratios do not depend on the TCS phase. The figures were produced from several runs with different latency settings, recorded with a low intensity beam to avoid bad signals from pileup<sup>1</sup>.

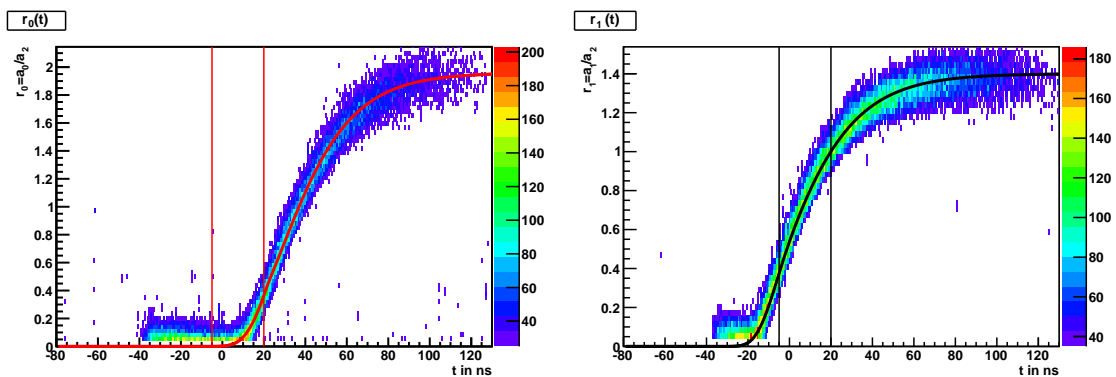


**Figure 4.2:** Latency scan of SI03Y in 2010 and corresponding reconstruction function. Artificial lines from low-amplitude noise were eliminated by adding random numbers between  $-1.5$  and  $1.5$ , and only bins with a number of entries above a certain threshold (25 for  $r_0$ , 35 for  $r_1$ ) are displayed. The lines mark the region where the detectors operate at nominal latency.

The **reconstruction function** introduced in 2004 by J. Friedrich [Fri10]

<sup>1</sup>When a second particle causes a signal in the same strip as the first, the amplitudes add up and are distorted. The resulting amplitude samples do not yield correct time information in the general case.

$$(4.3) \quad r(t) = r_0 \cdot \exp [-\exp [-s(t')]],$$

$$(4.4) \quad \text{with } s(t') = \left( \frac{a+c}{2} \cdot t' + \frac{a-c}{2} \left( \sqrt{t'^2 + b^2} - |b| \right) \right) + d$$

$$(4.5) \quad \text{where } t' = t - t_0$$

is a very convenient parametrization, since its parameter space is not too large, but sufficient to describe the signal as observed in the data. It can be inverted to give

$$(4.6) \quad t(r) = t_0 - s^{-1} \left( \log \left[ -\log \left( \frac{r}{r_0} \right) \right] \right)$$

$$(4.7) \quad \text{with } s^{-1} = \frac{1}{2ac} \left[ (a+c) \cdot f(x) - (a-c) \cdot \sqrt{f(x)^2 + acb^2} \right]$$

$$(4.8) \quad \text{and } f(x) = x - d + \frac{b}{2} \cdot (a-c),$$

which can be used to find the TCS phase for a hit in the detector. Since this function is also analytical, one can directly propagate the error of the amplitude measurement into an error in time. The reconstruction functions for both ratios are displayed with the latency scans in fig. 4.2.

With three amplitude samples, two independent ratios  $r_0$  and  $r_1$  are available to give time information. Assuming both ratios return valid times, for every signal two sets of time information are available. Errors in both times arise from the noise-induced uncertainties  $\sigma_a$  in the amplitudes, which are recorded regularly in dedicated *pedestal runs*. The error  $\sigma_{rx}$  of ratio  $x$  is calculated from the errors in the amplitudes over

$$(4.9) \quad \sigma_{rx} = \frac{a_x}{a_2} \sqrt{\left( \frac{\sigma_a}{a_x} \right)^2 + \left( \frac{\sigma_a}{a_2} \right)^2} = \frac{\sigma_a}{a_2} \sqrt{a_x^2 + a_2^2}.$$

When propagating this into an error in time, due to the curvature of the reconstruction function the errors become asymmetric. This is taken into account by introducing upward and downward errors:

$$(4.10) \quad \sigma_{tx}^+ = t(r_x + \sigma_{rx}) - t(r_x), \quad \sigma_{tx}^- = t(r_x) + t(r_x - \sigma_{rx})$$

The two times obtained from the ratios are merged into one *strip time* by creating the mean, weighted with the errors in the direction of the other time (i.e. for the smaller time, the upward error is taken).

$$(4.11) \quad t = \frac{t_1\sigma_0^2 + t_0\sigma_1^2}{\sigma_0^2 + \sigma_1^2}$$

The asymmetric errors for the strip time are calculated via error propagation:

$$(4.12) \quad \sigma_t^+ = \frac{1}{\sqrt{\frac{1}{(\sigma_0^+)^2} + \frac{1}{(\sigma_1^+)^2}}}, \quad \sigma_t^- = \frac{1}{\sqrt{\frac{1}{(\sigma_0^-)^2} + \frac{1}{(\sigma_1^-)^2}}}.$$

### 4.2.1 Signal shape

Defining the reconstruction function means defining the evolution of the signal amplitude with time as well. Every amplitude sample at a given TCS phase  $a(t)$  is linked to the following one  $a(t + \Delta)$  via the reconstruction function

$$(4.13) \quad \frac{a(t)}{a(t + \Delta)} = r(t)$$

(4.14)

More generally, a sample is related to a sample taken  $N$  clock cycles later by

$$(4.15) \quad a(t) = \left( \prod_i^{N-1} r(t + i\Delta) \right) \cdot a(t + N\Delta)$$

Additionally, the late part of the signal is known to be an exponential decay, as can be deduced from the fact that the reconstruction function approaches a constant value  $r_0$ . The coefficients of this decay are defined by  $r_0$ :

$$(4.16) \quad r_0 \cdot e^{-(t+N\Delta)/\tau} = e^{-(t+(N-1)\Delta)/\tau}$$

$$(4.17) \quad r_0 = e^{\Delta/\tau}$$

$$(4.18) \quad \tau = \frac{\Delta}{\ln r_0}$$

So every amplitude can be expressed as

$$(4.19) \quad a(t) = \left( \prod_{i=0}^{N-1} r(t + i\Delta) \right) e^{-(t+N\Delta/\tau)}$$

by choosing  $N$  in a fashion that  $a(t + N\Delta)$  is assured to be on the exponentially falling part of the signal.

Figure (4.3) displays the signal shapes reconstructed from the 2010 calibration for SI03Y from both ratio functions separately.

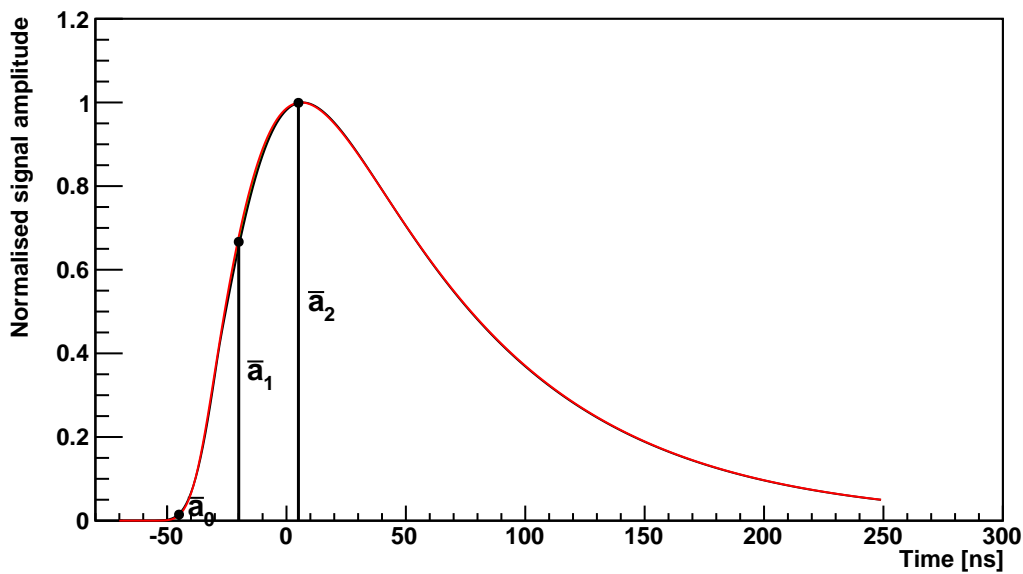


**Figure 4.3:** Signal shape, reconstructed from the 2010 time calibration of plane SI03Y. The mean position of the samples is marked on the curve.

### 4.3 Time Calibration

Time calibration is a procedure that needs to be performed for every readout plane of the silicon detectors at least once for every beam time. At best, this happens as part of the commissioning phase at the beginning of the beam time. As soon as the triggers - or at least the beam trigger - are calibrated, dedicated runs can be started for the time calibration of the scintillating fibers (SciFi/FI) and the silicon detectors. In order to properly calibrate the silicon detectors, calibrations for the SciFis should already be available, since they have excellent time resolution in the order of 300 ps and are therefore highly useful to define the time of a track in the beam telescope.

The first step is to perform a latency scan, where in several runs, planes are operated at different latency settings around the value that will be the nominal setting during data taking (which can be assumed to be the same as in the previous year as long as no trigger time shift took place). To record the full evolution of the ratio along with the TCS phase as in fig. 4.2, a region of approximately 200 ns, corresponding to 8 different latency settings, should be covered. In order to have good track reconstruction, half of the planes are always operated at nominal latency while that of the other planes is changed. To get a clearer signal, a low intensity beam of about  $1 \cdot 10^6$  particles per spill is used where pileup is virtually non-existent.

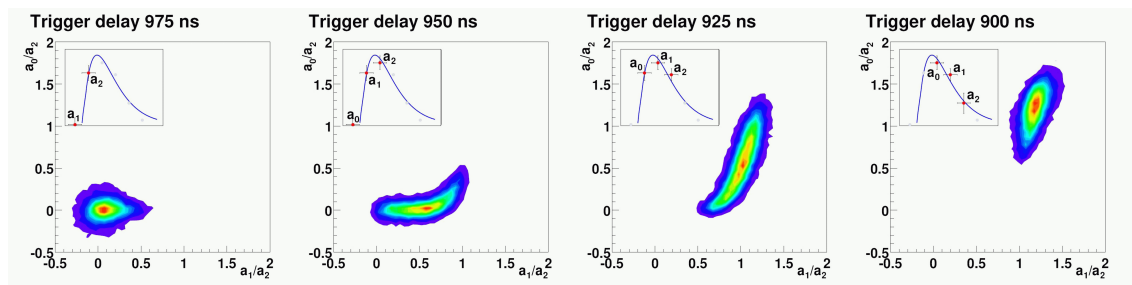


**Figure 4.4:** Distribution of  $r_0$  vs.  $r_1$  for different latency settings, from [Wag01]. The position of the samples with respect to the signal is given. For a too large latency, only  $a_2$  lies on the rising edge of the signal and the ratios are zero. For a too small setting, all samples are on the falling edge and the ratios reach a constant value. The second panel shows a correctly adjusted latency.

After the latency scan, every plane is set to its nominal latency, which may also need to be adjusted at the beginning of a beam time. That means, the latency needs to be set in a way that the  $r_0$  values are situated just on the rising edge of the signal, while  $r_1$  is not yet at its maximum (cf. fig. 4.4).

Time calibration for the silicons means determining the parameters of the reconstruction function (4.3). Assuming the signal shape does not change within one beam time, which was found to be true within sufficient limits by performing a latency scan at the beginning and at the end of a beam time, the parameters need to be determined only once per year, with the exception of the time shift  $t_0$ , which should be checked regularly (cf. section 4.3.1).

Up until 2009, the calibrations were produced quasi-online, using COOL with its rudimentary track fitting method and a designated calibration toolkit written by A.-M. Dinkelbach [Din11]. Since there is usually no proper alignment file available at the time of the latency scan - partly because a good alignment requires at least rudimentary time calibration - a pre-alignment of the beam telescope had to be created iteratively, its quality being judged by the  $\chi^2/ndf$  of the reconstructed tracks. When this was finished, one could cut on  $\chi^2/ndf < 10$  and have low-background histograms to fit. Subsequently, the two-dimensional ratio vs. TCS phase histogram is fitted by fitting gaussian distributions to one-dimensional slices of the two-dimensional histogram and then fitting the

reconstruction function through the means values of the previous fits.

This method was found to produce "bad" calibrations for cryogenic detectors in a way that the parameters  $a$  and  $c$  became very small in the fit (in the order of  $10^{-14}$ ), which resulted in overflows in the implementation of the reconstruction function. Thus, another approach was chosen by creating preliminary calibrations with COOL, that suffice to create a proper alignment, and final calibrations offline, using Coral. One advantage of this process is that for a preliminary calibration, it is sufficient to make the reconstruction function fit the ratio/TCS phase histogram without considering track times, which removes the necessity of calibrated SciFis. The fitting of the final calibration to the curve has to be done, starting from the preliminary calibration, "by hand" using a tool written by Jörg Martin [Mar09] that allows to change the parameters as part of a ROOT macro, then drawing the reconstruction function into the latency scan (or any other ratio vs. TCS phase histogram).

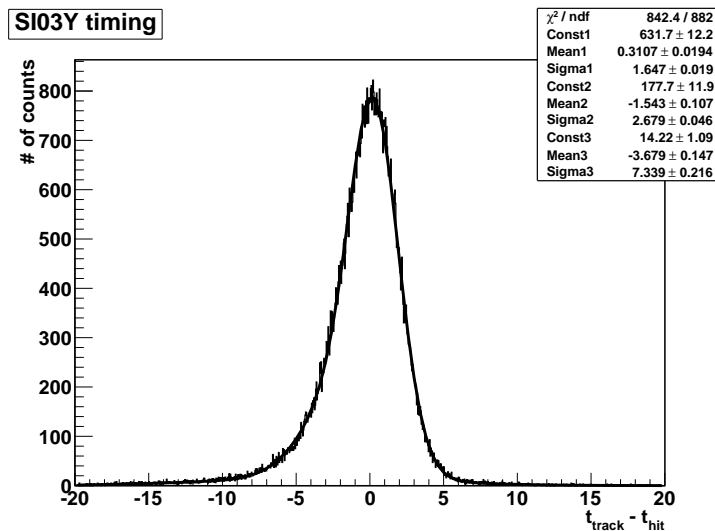


**Figure 4.5:** Distribution of offsets between hit and track time for SI03Y in hadron run 76860 (2009), after completed time calibration. The distribution can be fitted by three gaussian distributions, which can be identified with cluster sizes one to three (the fraction of bigger clusters is negligible). The main contribution, from cluster size one, has a mean width of  $\sigma = 1.65$  ns.

Once the signal shape is defined, only the signal start parameter  $t_0$  needs to be shifted in a way that the mean of the  $t_{\text{track}} - t_{\text{hit}}$  distribution lies at zero. This one-dimensional histogram (fig. 4.5) can be easily fitted by a gaussian even with low statistics ( $\sim 30000$  events) and the calibration's  $t_0$  is shifted automatically for all readout planes in one go.

### 4.3.1 "Jumping" time calibrations

For 2009 data, some of the detector planes were found to show an unexpected behaviour. The time shifts that seemed to be stable within a precision of about 3 ns in earlier years, now showed deviations of 12 ns on several occasions, for one readout plane even on a

regular basis. The shifts did not seem to slowly wander to this value, but to jump there between spills.

Considering that, within the precision of the detector, the value of the jump seems to be exactly one half TCS cycle, the problem is expected to occur in the readout chain, in particular the ADC card. It is, however, hard to narrow this down further without spending enormous amounts of time on the firmware of the whole readout chain and observation of the timing, since the jumps appeared on a time scale from several days to a few weeks. The problem also did not seem to be conclusively cured by reloading the readout chain, i.e. in some cases upon a `LOAD` command, a jump back occurred, in others it did not. It is, however, hard to distinguish between a "jump" and a "jump back", considering the intermediate times are of a similar scale.

As it is not foreseen in Coral to change calibrations within a run, it was necessary to introduce a new type of calibration for the silicons, which is spill-specific and shifts  $t_0$  by a multiple of a half TCS cycle whenever necessary. These calibrations were produced using the online filter Cinderella, as it is sufficient to determine the timing of the majority of digits with a precision of a few nanoseconds. Cinderella can provide this without need for tracking, which would significantly slow down the process.

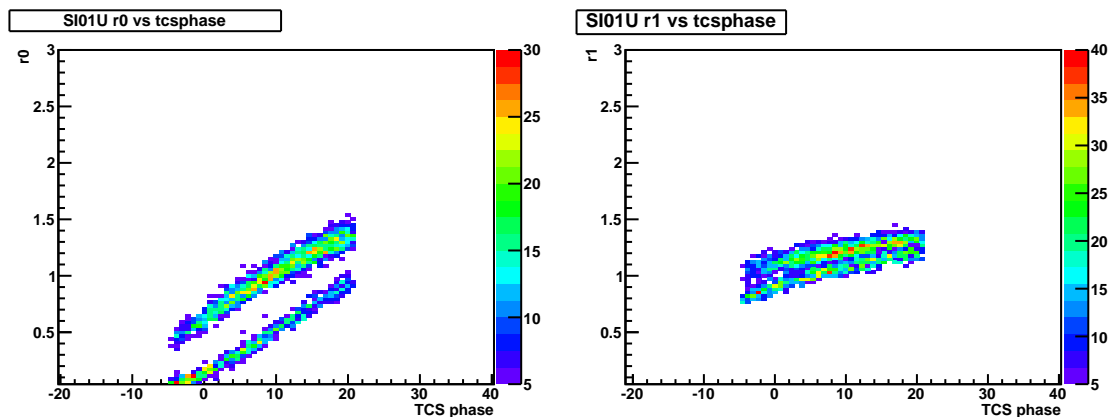


**Figure 4.6:** Ratio vs. TCS phase histograms for SI01U in run 77918, events from the first and last three spills. Within the run, the detector plane shifted its readout latency by half a clock cycle.

Running Cinderella on *lxbatch*<sup>2</sup>, it streams data from CASTOR, processes it spill-by-spill and gives histograms displaying  $t_{hit} - t_{tcs}$  to the *calibrator*, a cinderella tool that was designed for online detector calibrations. It is equipped to find the peak position in a histogram by summation over a predefined number of bins - corresponding to the peak width - and returning the value with the highest sum. For this to be significant in any way, a valid time calibration has to be available. The calibrator writes to an output file whether a jump occurred in the considered spill. This file can later be converted to a cali-

<sup>2</sup>The CERN computing cluster

bration file, containing only the run and spill number where a jump occurred.

The current implementation is thought mostly for offline usage on lxbatch or lxplus, for online application more effective implementation of the code is still due.

Even after this correction has been executed, effects of the jumps can still be observed in megaDST data: the distribution of the ratios in dependency of the TCS phase shifts with the jump as in fig. (4.6).

## 4.4 Clustering

Once the time information for one event has been extracted for all strips, they need to be merged to clusters.

### 4.4.1 Finding regions and splitting into clusters

At first, all digits<sup>3</sup> need to be separated into groups of neighbouring strips with a signal (*regions*). The digits are submitted to the clusterization method unordered and are first sorted by wire number. Following this, regions are created as sequences of digits with consecutive wire numbers. Inside a cluster, a *consistency* is calculated for all neighbouring strips according to the formula

$$(4.20) \quad c = \left| \frac{t_1 - t_2}{\sqrt{\sigma_1^2 + \sigma_2^2}} \right|,$$

where the asymmetric errors for  $t_1$  and  $t_2$  are chosen in a way so they point toward the other time (i.e. for the smaller time, the upward error is chosen). This consistency value is a measure for how far apart the times calculated for the two strips are, and thus whether both digits could result from the same particle crossing the detector.

These regions can then be splitted into actual clusters by walking along every digit and examining it for finity of the calculated time, consistency value with the previous strip and, naturally, whether another strip follows in this region. The upper limit for the consistency, above which strips are torn, is hard-coded to a value of 3.5 in Coral.

For clusters of size two or more, a new timing is calculated from the sums of the amplitude samples in the same fashion as the time for the single strips was calculated. It was discovered (cf. [Din11]) that the cluster times' deviation from the track times depends on the cluster size. The time reconstruction algorithm was thus modified, using two parameters in the time calibrations that were remnants of a redundant implementation of a former linear time reconstruction and set to zero for all calibrations after 2002.

---

<sup>3</sup>information on a event from a single strip is stored on CASTOR as *digits*

Though the clustering algorithm is not limited on cluster size, clusters of size one and two dominate the data. Since the charge cloud produced by a passing particle has a diameter of about  $1\ \mu\text{m}$ , which is much smaller than the pitch between the wires, this is to be expected. The small percentage of real clusters with a size 3 or more results from the creation of  $\delta$ -electrons that traverse the wafer and create more charge carriers.

Neighbouring clusters with equal timing within the consistency limits can not be reliably distinguished, and are thus combined to one big cluster. Especially for events with outgoing particles in the very forward direction, with small angles between the trajectories, like the conversion of a high-energetic photon into a  $e^+e^-$ -pair, this affects the reconstruction efficiency on the software-level in a negative way. This limitation was improvisationally solved by splitting clusters of size 3 and more into several clusters if there is more than one peak in the amplitude series. In the 3-strip case, the amplitude of the intermediate smaller strip is split up into both clusters: half of the amplitude produced in the middle strip is accounted to each cluster.

#### 4.4.2 Cluster position

The cluster's position in the detector is calculated as a mean of the wire numbers, weighted with the respective strip's amplitude. Clusters with only one strip are thus simply attributed the position of its wire, while for those with two strips  $n$  and  $n + 1$ , a charge fraction  $\eta$  is calculated:

$$(4.21) \quad \eta = \frac{a_{n+1}}{a_n + a_{n+1}}$$

This yields more precise information on the hit position. In a first approach, the cluster position  $h$  was simply given as

$$(4.22) \quad h = h_n + \eta \cdot d,$$

where  $h_n$  denotes the position of wire  $n$  and  $d$  is the pitch between the wires.

Figure 4.7 displays the distribution of  $\eta$  for two-strip clusters. On the p-side, the distribution peaks at 0.5: the intermediate strips collect the charge, and by capacitive coupling strips on both sides receive an equal amount of charge. When the fraction approaches zero or one, the number of entries declines rapidly: Almost all charge is collected in one strip, the amplitude in the other strip is eliminated by the ADCs zero suppression and the cluster ends up as a single strip.

By looking at this distribution, the conclusion that the cluster position does not scale linearly with  $\eta$  is obvious. The dependency was determined empirically by fitting a polynomial to the distribution of residuals over values of  $\eta$  (by assuming a linear relation

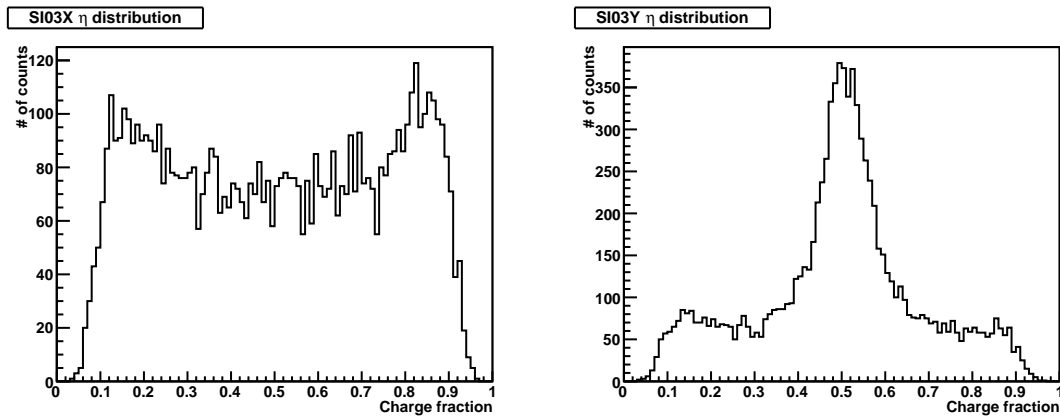


**Figure 4.7:** Distributions of the charge fraction  $\eta$  for n- (left) and p-side (right) for detector module SI2.01 in 2010 (SI03XY, 200000 events from run 84112). For the p-side with intermediate strips, charge sharing is favoured. Only two-strip clusters were considered.

between  $\eta$  and cluster position at first) and a corresponding correction was implemented into the reconstruction [Din11].

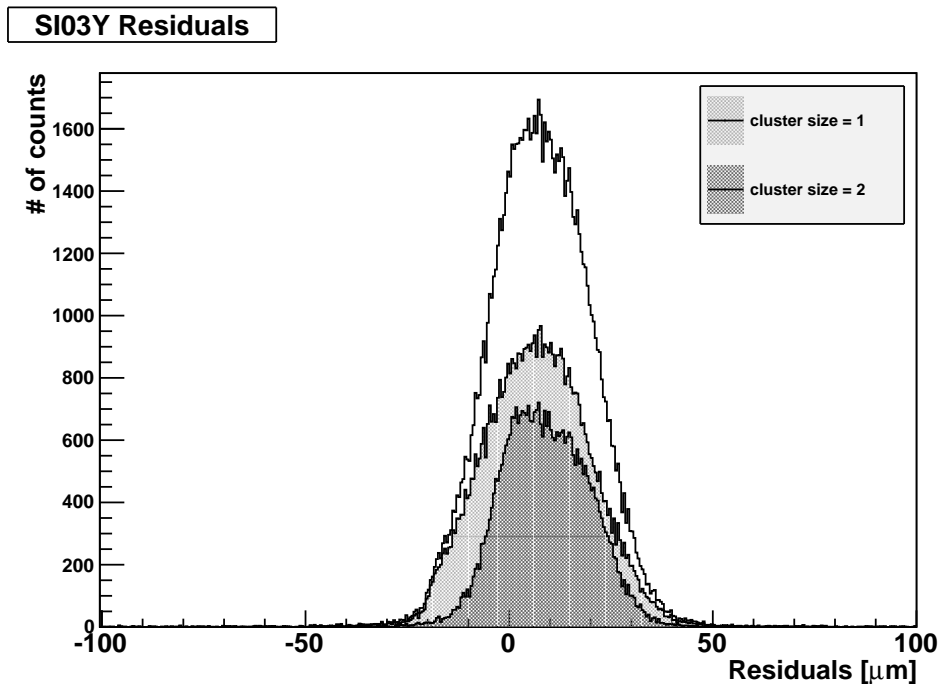


**Figure 4.8:** Distribution of residuals for plane SI03Y in run 76860, for cluster sizes 1 and 2.

The result is a spatial resolution in the order of 8 – 12  $\mu\text{m}$ . It depends on cluster size, since with two-strip clusters the usage of information included in the charge sharing yields a higher precision than the one-strip case.

## Chapter 5

# Performance of the detectors in cryogenic and non-cryogenic operation

While non-cryogenic operation of the detectors is easier to maintain, there are several advantages to cold detectors. In addition to the recovery from radiation damage, time resolution can be significantly improved if properly taken care of. Starting 2009, the silicon detectors were operated in a cryogenic state. For details, see section 3.3. In the following chapter, a brief overview on both hardware during data taking and detector analysis for both cryogenic and warm operation, for muon and hadron beam respectively, is given. For hadron beam, detector module SI1.08 is chosen as a comparative sample. It was used in both 2008 and 2009 inside the conical cryostat, though the position was changed from SI04XY to SI05XY. For muon beam with cryogenic detectors, one of the Primakoff muon test runs from end of 2009 (run #81993) is chosen. Unfortunately, from 2007 and earlier muon beam times, no detector modules were used for the cryogenic operation, thus direct comparison is not possible.

Performance histograms for all detector planes in 2009 can be found in appendix B.

### 5.1 Hardware

#### 5.1.1 Cooling system

In non-cryogenic operation, the detector stations are flushed with gaseous nitrogen, at a rate of about 300 – 500 l/h. Since there is no automatized regulation of the flows, which instead stay essentially constant on a short-term scale, the flows need to be checked by the shift crew regularly to ensure long-term functionality. The thermal connection to the "outside world" results in fluctuations of the detector temperatures on a day-night scale as well as along with general weather conditions. These fluctuations have a direct impact

## 5 PERFORMANCE OF THE DETECTORS IN CRYOGENIC AND NON-CRYOGENIC OPERATION

on data quality, as will become visible in section 5.2. In 2008, temperatures of the modules inside the conical cryostat varied between 322 K and 330 K during data taking.

In cryogenic operation, the nitrogen flow is regulated according to the temperature development and thus the temperature can be kept stable with fluctuations lower than 1 K. On the other hand, the regulation software is prone to errors and detector experts need to be able to handle the system, and in case of a problem, act quickly in order not to lose beam time.

### 5.2 Tracking performance

#### 5.2.1 Amplitude and noise levels

The noise level corresponds to the standard deviation of the pedestal value for a single strip and is in the order of 1 – 2 ADC channels for a fully depleted sensor with no or low radiation damage. For the modules that were used in the beam telescope from 2001 to 2007, the noise went up to about 4 ADC channels in the center of the detector, where most beam particles pass and most of the energy is deposited.

The radiation-induced lattice defects not only increase the leakage current, they have an influence on the charge collection efficiency as well. Defects can act as acceptors for charge carriers, releasing them again after a time that is typically longer than the readout time of the detector. This way, the charge is lost from the signal amplitude. Lower amplitudes result in higher relative uncertainties in both spatial and time resolution. With a lower temperature of the wafer, the chance that the defect already has all its niveaus occupied increases. Thus, the rate of lost charge carriers from a signal gets lower and the lost charge collection efficiency can be partially regained. For module SI1.08, the most probable value (MPV) of the cluster amplitude in september 2008 (in non-cryogenic operation) was 44 ADC channels for the p- and 46 channels for the n-side, while in cryogenic operation in 2009, the most probable cluster amplitudes were 52 and 56 channels.

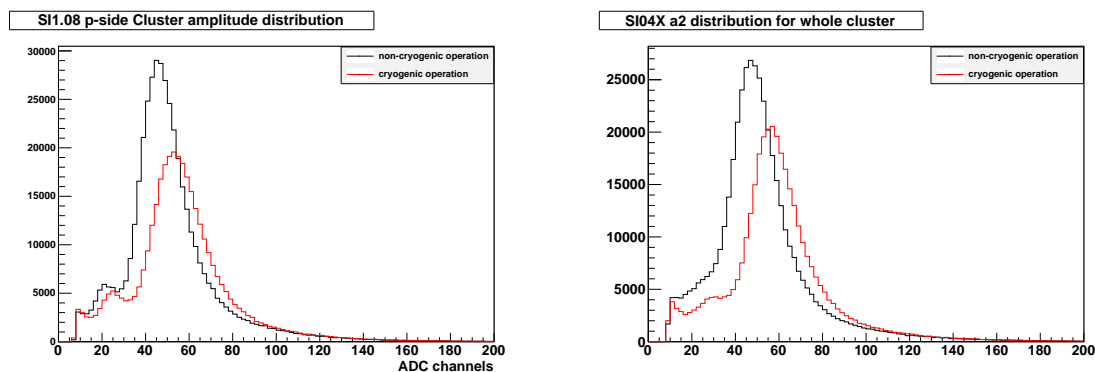


**Figure 5.1:** Cluster amplitudes of detector module SI1.08 p- (left) and n- side (right) in cryogenic and non-cryogenic operation.

### 5.2.2 Signal shape and time resolution

With the temperature of the detector, the temperature of the APV chips changes as well. This alters the properties of the shaping circuit, and thus the shape of the signal. With the temperature of the sensor at 200 K, the APV temperature was still comparatively high ( $\sim 265$  K). Nevertheless, the behaviour changed noticeably, having an impact particularly on the time calibrations. The most distinctive change was that of the maximum of the ratios  $r_{0i}$ , which increased from  $r_{00} \sim 1.5$  and  $r_{01} \sim 1.22$  to a value of  $r_{00} \sim 2$  and  $r_{01} \sim 1.43$  (the values vary with the detector planes). The maximum ratios are directly connected to the decay time  $\tau$  of the signal via eq. (4.16). Thus, the decay time for non-cryogenic detectors can be estimated to  $\tau_{nc} \sim 127$  ns while for non-cryogenic detectors, it is  $\tau_c \sim 74$  ns.

The topic of time resolution is closely related to the signal shape: a shorter signal corresponds to a higher maximum value of the ratio functions. At the same time, the width of the inclination remains approximately the same ( $\sim 70$  ns). Accordingly, the same error in amplitudes will lead to a smaller error in time for a cryogenic detector, where the slope of the reconstruction function is steeper.

As a consequence, time resolution in cryogenic operation could be improved to a value of  $\sim 1.4$  ns in the best cases (SI01X, SI03U) for both muon and hadron beam and 2.5 ns in the worst case for muon beam, while the worst resolution in hadron beam was around 2.2 ns (SI03V). In comparison, for non-cryogenic operation the resolution varied from 1.8 ns in rare cases in hadron beam for the n-side of the detectors to 3.0 ns for the p-sides, and about 1 ns worse (2.8 ns for n-side and 4 ns for p-side) in case of muon beam.

Looking at the timings for cluster sizes one and two separately (fig. 5.3 middle), it is visible that both cases form separate gaussian distributions with distinct mean values, which differ by up to 2 ns, mostly on the p-sides of the detector. This effect could be accounted for by including the offsets into the time calibrations. As a result, time resolutions improved by a factor of up to 10 %, especially for planes with a previously bad timing. In particular, the width of all distributions could be brought below 2 ns for hadron beam.

### 5.2.3 Charge sharing and residuals

In 2008 data and afterwards, an unanticipated effect occurred: readout planes on the n-side were found to have a distribution of the charge sharing coefficient  $\eta$  similar to that of p-sides, where the intermediate strips enhance charge sharing and the distribution peaks around 0.5 (cf. section 4.4.2). It was found that all modules that showed this behaviour were from the 2008 production of sensors (SI1.xx), which led to the conclusion that they had a modification in design to the other sensors (for the "standard" design, see sect. 3.2.2): instead of the p-stops, preventing short circuits on the n-side strips, a different approach was chosen by applying a *p-spray*-layer, which allowed a placement of intermediate n-strips that was not possible with the p-stop technology. The affected detectors are all of SI04 and SI05 in hadron beams 2008 and 2009, as well as all modules of SI02 in 2009 and 2010.

## 5 PERFORMANCE OF THE DETECTORS IN CRYOGENIC AND NON-CRYOGENIC OPERATION

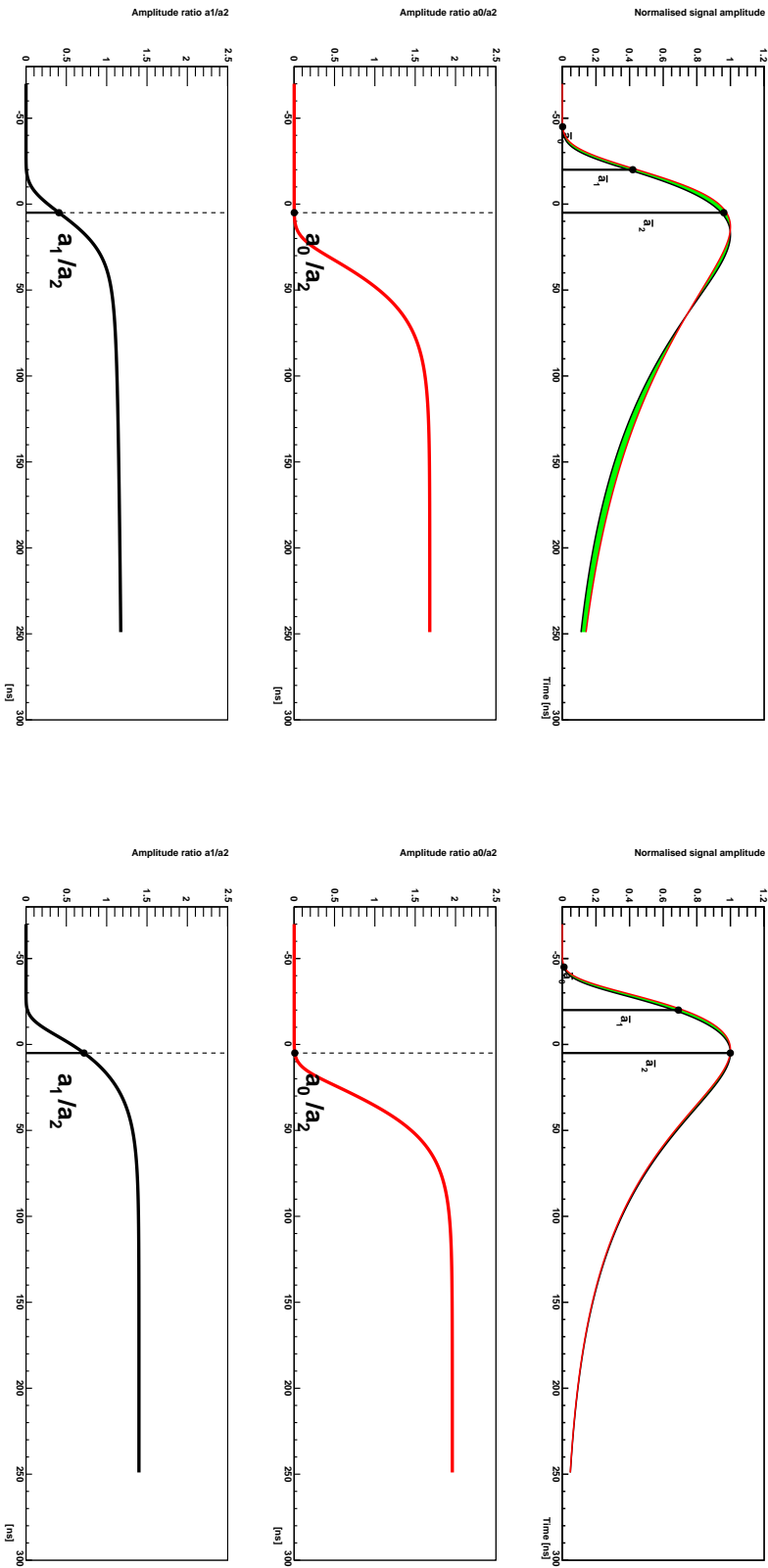


**Figure 5.2:** Signal shapes and ratio functions for non-cryogenic (left) and cryogenic(right) detectors. In both cases, the red curve was reconstructed from the  $t_0$  and the black curve from the  $t_1$  calibration.

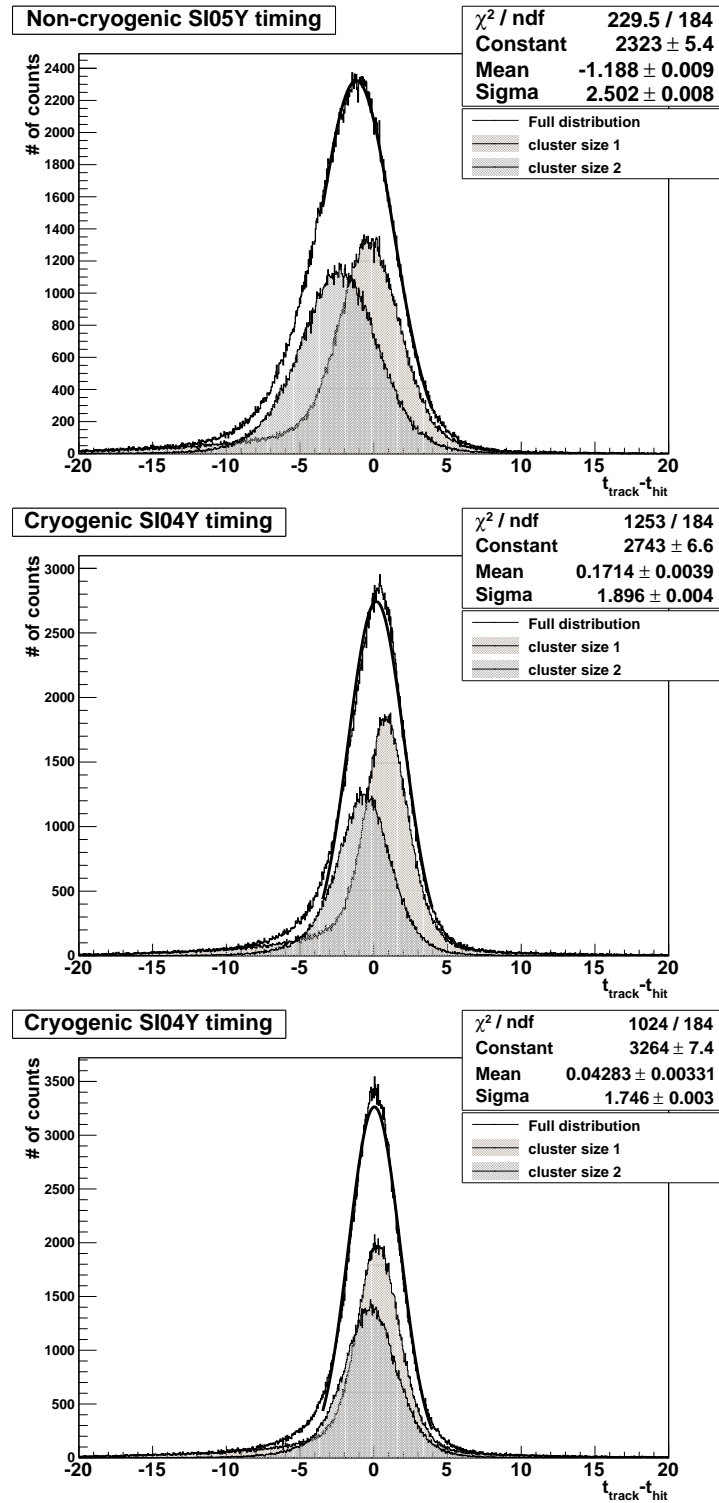


**Figure 5.3:** Timing of the p-side of module SI1.08 in non-cryogenic (top) and cryogenic operation(middle), and with the correction by cluster size applied (bottom) for hadron beam.

## 5 PERFORMANCE OF THE DETECTORS IN CRYOGENIC AND NON-CRYOGENIC OPERATION

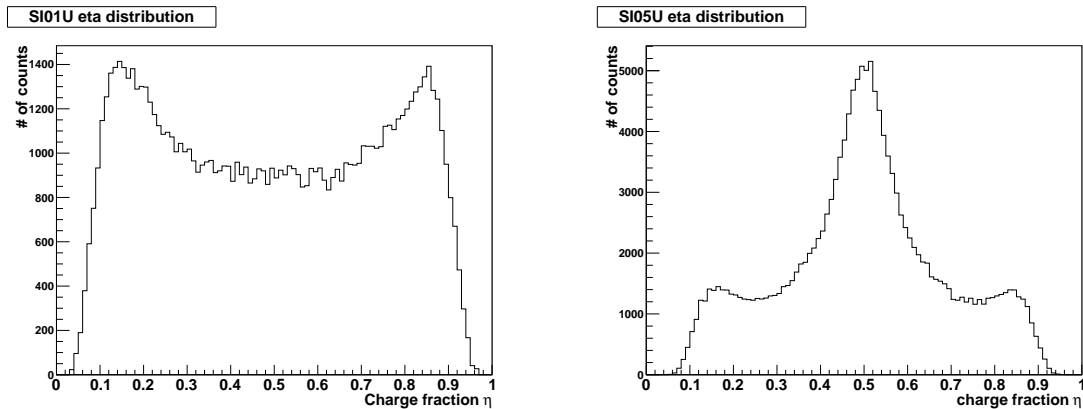


**Figure 5.4:** Distribution of the charge fraction coefficient  $\eta$  for module SI2.02 (left) and for SI1.12 (right). The different behaviour of the SI1.xx production due to intermediate strips on the n-side is obvious.

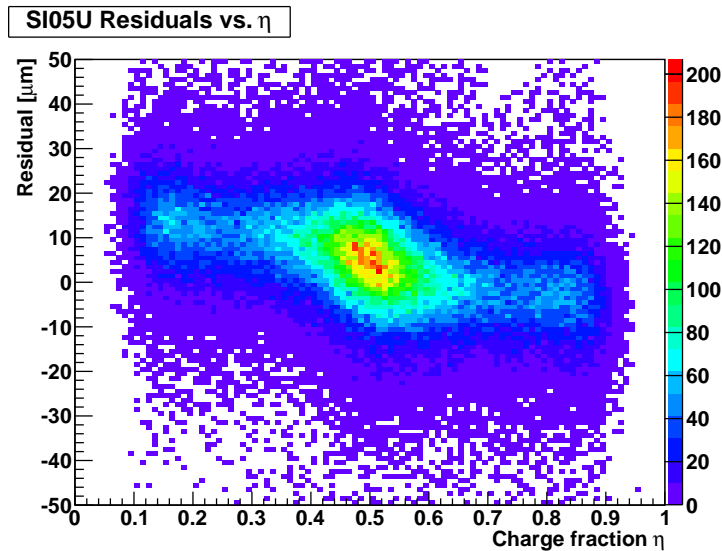


**Figure 5.5:** Distribution of residuals over the charge fraction coefficient  $\eta$ . As the presence of intermediate strips on the n-side was not anticipated, the correction for  $\eta$  was applied incorrectly and the residuals are  $\eta$ -dependent.

As these module properties were not known until recently, no measures to compensate for this in the reconstruction software were taken yet. This necessarily resulted in errors in spatial resolution, as can be easily seen in figure (5.5): the mean residual would, in the optimal case, be zero for all values of  $\eta$ . Instead, it remains at a near-constant value around  $+11 \mu\text{m}$  where  $\eta \in [0, 0.4]$  and  $-9 \mu\text{m}$  for  $\eta \in [0.6, 1]$ , the transition in between occurs in the bulk around 0.5, where most hits appear. As a consequence, spatial resolution appeared to be comparatively bad for several planes from 2008 to 2010. However, with the effect known, this can be compensated for.

Mean resolutions in hadron beam were around  $13 \mu\text{m}$ , with two-strip clusters varying

from  $5\ \mu\text{m}$  to  $12\ \mu\text{m}$  and one-strip clusters from  $11\ \mu\text{m}$  to  $15\ \mu\text{m}$  in both cryogenic and non-cryogenic operation, cf figure 5.6.

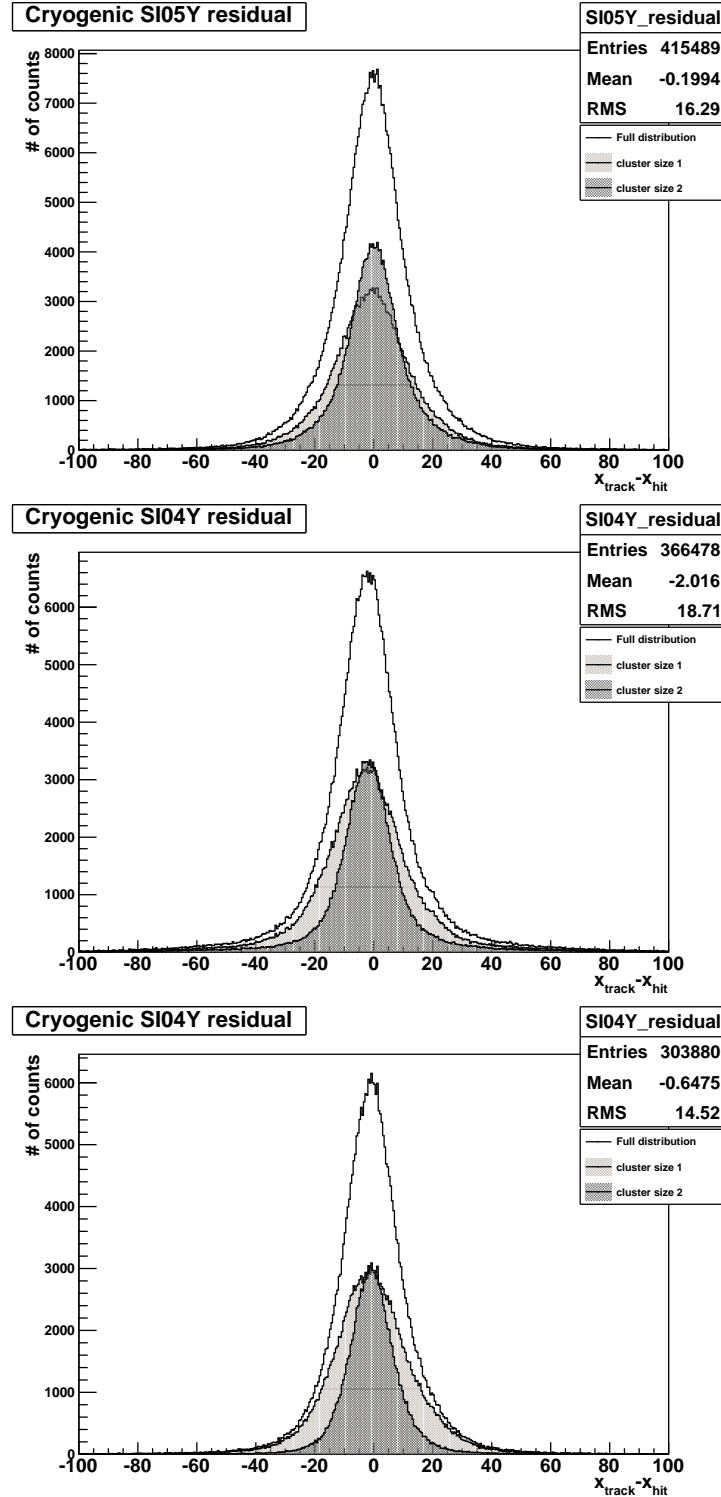


**Figure 5.6:** Residuals of SI1.08 n-side in non-cryogenic (top) and cryogenic operation (middle) in hadron beam, and for cryogenic operation in muon beam

#### 5.2.4 Tracking (Pseudo-)Efficiency

A detector plane's tracking efficiency is defined as the fraction of tracks crossing the detector for which a corresponding hit is found. If the plane itself contributed to the tracking process, the result is only a pseudo-efficiency. The obtained values depend on beam intensity: in a high-intensity beam pileup will result in wrong reconstruction of both time and position of the hit. The hit will not be associated to its track - thus, efficiency will decrease.

Efficiencies can be generated as a full detector efficiency value, or for single or small groups of strips in a 2D histogram. Detector efficiencies are, in usual cases, around 99 % in a full intensity hadron beam ( $\sim 10^6$  particles per spill) and 95 % in muon beam ( $\sim 2 \cdot 10^8$  particles per spill). Locally, efficiencies can, in single cases, go below 70 % in strips where the baseline shifted and the detector delivers a constant noise signal. Excluding the case of noisy strips, local efficiencies usually are above 80 % in muon beam. In hadron beam, local efficiencies of the beam telescope are virtually always above 90 %, while in the vertex detector, high particle multiplicities cause lower efficiency in the order of 80 % locally.

Although intuition may suggest that due to shorter signal decay times, the rate of pileup would be diminished, this does not hold up at least for hadron beam: pileup is mostly caused via the decay of produced particles, or production of hadronic showers. So pileup in hadron beam is caused by events with high multiplicities and/or small angles, and is thus not related to signal decay time and time between incoming beam particles, at least at rates the hadron beam delivers.

In muon beam, however, where beam intensity is two orders of magnitude larger and average times between incoming beam particles are in the order of 5 ns, while interaction rate is lower, part of the inefficiency can be explained with pileup from successive beam particles, i.e. one would expect the efficiency to improve with cryogenic detectors and shorter decay times.

Unfortunately, the 2007 alignment proved not to be sufficiently reliable to produce efficiency histograms that allow any significant conclusion.

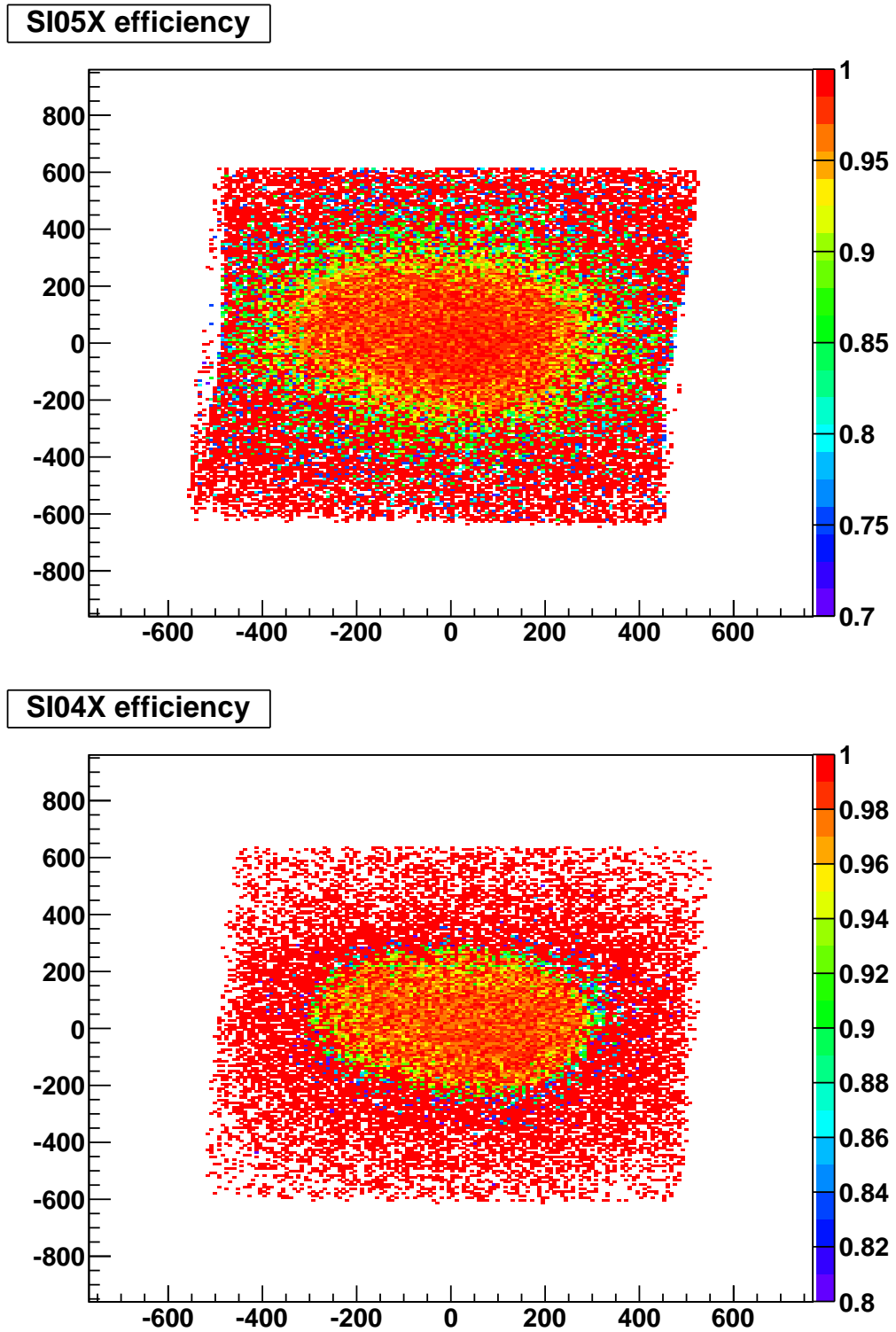


**Figure 5.7:** Pseudo-efficiency of the p-side of module SI1.08 in hadron run 2008 (non-cryogenic operation, top) and 2009 (cryogenic operation, bottom)



# Chapter 6

## Alignment studies

### 6.1 The alignment procedure

In order to have a precise reconstruction of events, positions of all detectors need to be known with the best achievable precision, which is in the order of the respective detector's resolution. This includes coordinates of the detector centers, rotation angles, pitches between single channels and some constant parameters like detector size and number of channels.

The positions of the detector stations are recorded at the beginning of a beam time by a surveyor team of the CERN EDMS<sup>1</sup> [EDM] with a precision in the order of  $0.1 \mu\text{m}$ , the position of the actual detectors can then be deduced from technical drawings.

To increase the precision, before physics data taking a dedicated *alignment run* is taken: The beam is set to low intensity, some detector dead zones (e.g. GEMs) are switched on and the beam is defocused by leaving two focussing quadrupole magnets off. Data is taken in two runs, each about 30-40 spills, one with the spectrometer magnets off, the other with magnets on [Log]. This procedure is performed before every data taking period at COMPASS to account for potential small shifts of detectors resulting from work on the hardware.

The data recorded from an alignment run is used offline to create more precise alignment information. With the given position information, a first tracking with MegaDST output is processed, and using the  $\chi^2$  distribution of all tracks and its gradient, the detector positions are changed in the alignment file. As a cross check, the *pulls*<sup>2</sup> are expected to center around zero in a correct alignment.

This way, for all tracking detectors, the x- and y-coordinates as well as the pitch is adjusted. Due to the strong forward direction of the tracks, it is hard to adjust the z-positions

---

<sup>1</sup>Engineering & Equipment Data Management Service

<sup>2</sup>A pull is the distribution of residuals for a single detector plane, sometimes the mean value of this distribution is referred to as the pull as well.

of the detectors, which is why they are fixed in the standard alignment procedure, and remain in the position that was given in the alignment procedure.

## 6.2 z-realignment studies of the conical cryostat

### Motivation

A first glimpse at a test production of the 2009 Primakoff run showed several discrepancies in the vertexing:

- Target "position": The main target (nickel foil) as seen in the reconstructed vertices can be recognized as a peak in the z distribution of the vertices. This peak was found at a z position of  $-73.11$  cm, although it was constructed to be at  $-70$  cm<sup>3</sup>.
- Target "shape": Naïvely, one would expect to see the target as a symmetric distribution in the vertices, possibly described by one single gaussian, or several gaussians with a coinciding mean, taking into account different detectors and acceptances. The distribution that was actually found was describable by two gaussians, however the means diverged by  $1.7 \pm 0.03$  cm.
- Position of SI04: Just as the target foil, the position of SI04 can be extracted from the vertex distribution. It was found that the positions of the single modules diverged from those in the used alignment file by 2 and 4 mm, respectively (the modules were reconstructed at  $-11.9$  and  $-11.0$  cm, while the associated vertex peaks were found at  $-11.7$  and  $-10.6$  cm). For SI05 that kind of statement could not be made, as the following detectors could not sufficiently resolve the vertices to distinguish the single modules.
- Vertex vs. track angle: When histogramming the z position of the vertices against the angle of the outgoing track, a small slope of the distribution was visible. The actual vertex distribution should be independent of those angles and depend only on material budget along the beam axis.

### Changes and results

Since the problem seemed to include a major discrepancy somewhere in the alignment, it was decided not to use the standard alignment procedure with z positions freed to change, since this automatized approach is on the one hand only thought for minor shifts of about 1 mm, and on the other hand vulnerable to land in a local minimum of the mean track error, which is the criterium that is used to fit the parameters. Instead, a improvisational approach was chosen by using several samples of changed geometry,

---

<sup>3</sup>The origin of the COMPASS coordinate system for hadron runs is defined by the RPD, which surrounds the target. Thus, the target position is fixed by the construction.

shift	target position	mean <sub>1</sub> -mean <sub>2</sub> of target
-3 mm	-73.6 cm	2.0 cm
±0 mm	-73.1 cm	1.7 cm
+3 mm	-72.8 cm	1.5 cm
+13 mm	-70.5 cm	0.4 cm
+16 mm	-70.9 cm	0.6 cm
+19 mm	-71.3 cm	0.8 cm
+20 mm	-70.4 cm	0.4 cm
+21 mm	-70.3 cm	0.3 cm
+22 mm	-70.1 cm	0.2 cm
+24 mm	-69.9 cm	0.1 cm
+26 mm	-69.6 cm	0.04 cm
+28 mm	-69.3 cm	-0.2 cm
+38 mm	-68.0 cm	-0.9 cm
+52 mm	-68.0 cm	-2.0 cm

**Table 6.1:** Results of z realignment of the CC

namely shifting the positions of the detectors in the conical cryostat (i.e. SI04 and SI05) along the z axis. The improvement or degradation of the track quality was judged by means of the z distribution of the primary vertices, especially the criteria that displayed the discrepancies in the test production.

The first results pointed to an improvement at a shift of +20 mm, more thorough investigation gave a shift of +26 mm downstream. Most significantly, the target vertices occurred at -69.6 cm and the two gaussian means nearly coincide. Moreover, the vertices associated with the position of SI04 are in agreement with the positions in the alignment file. At the same time, the number of reconstructed vertices increased by 10%.

## Conclusions

It is so far not conclusive whether the received results are a final. The conical cryostat being positioned inside the RPD with a fixed geometry, there is actually no room for a discrepancy of this order of magnitude. Drawings and calculations have been triple-checked, at the same time a proper alignment procedure was executed with the positions of SI04 and SI05 shifted by both 20 and 26 mm. First results seem to support the shift, showing improvements to alignment problems between Silicons and Micromegas that could not be solved before [Aus10].

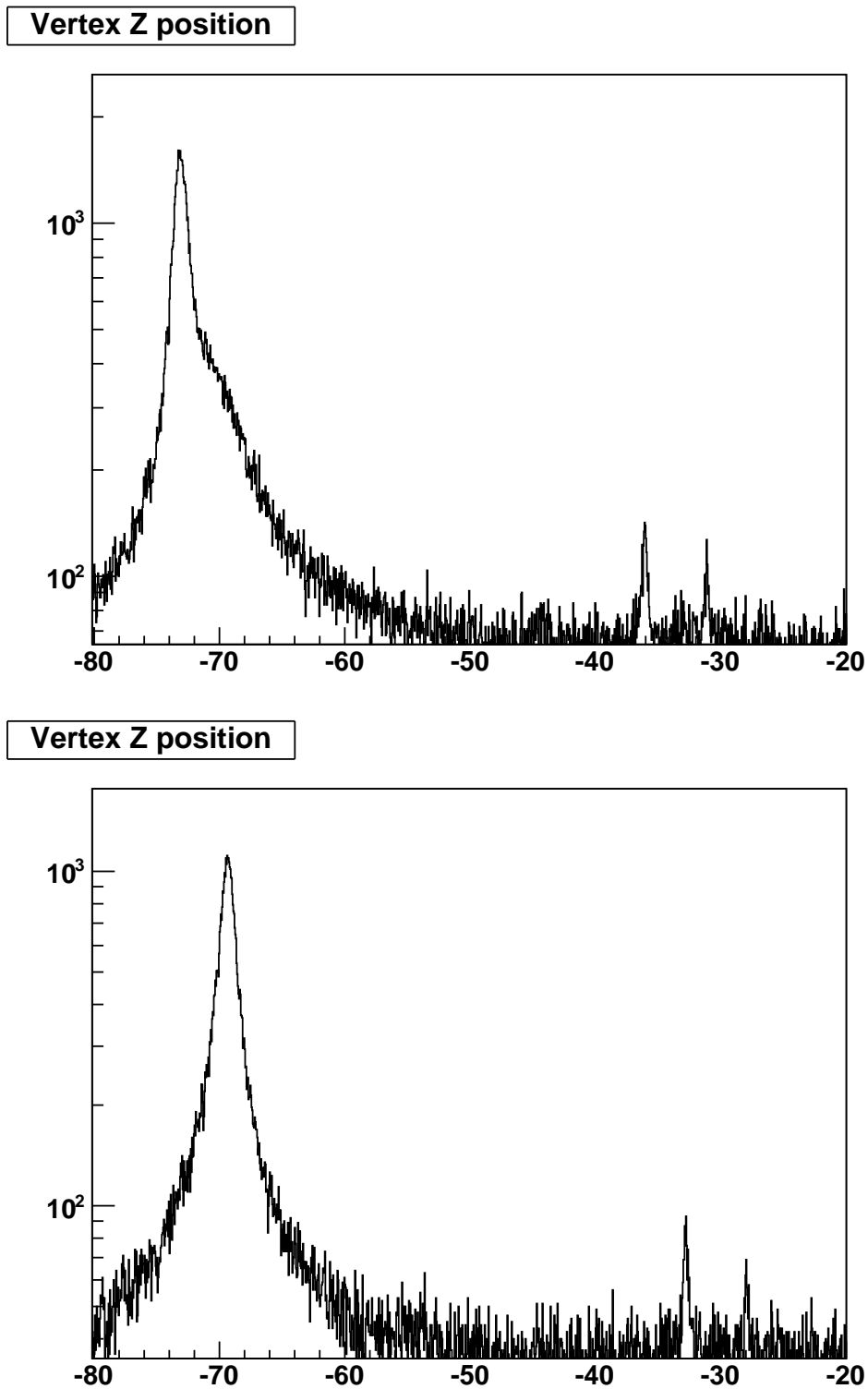


**Figure 6.1:** Distribution of vertices along the beam axis, in the target region, before (top) and after (bottom) re-alignment. The big peak, resulting from the main target foil, improves in position and symmetry. Also visible are the secondary targets at  $-36$  and  $-31$  cm before and  $-33$  and  $-28$  cm after the re-alignment

# Chapter 7

## Conclusion

### 7.1 Results

After two years of constant operation of the detectors in a cryogenic state, first results indicate a success of this development:

	Cryogenic	Non-cryogenic
Temperature deviation	$\pm 1$ K	$\pm 4$ K
Spatial resolution	13 $\mu\text{m}$	13 $\mu\text{m}$
Max. Time resolution	1.35 ns	1.8 ns

**Table 7.1:** Summary of properties of cryogenic and non-cryogenic detectors

Along with the initial goal of diminishing radiation damage, that will require some more investigation on a long-term scale, the above-mentioned advantages highly favour the continuation of cryogenic developments.

### 7.2 Outlook

Not the complete potential of the available information is implemented for the reconstruction of the silicon detectors yet. A reliable way needs to be found to distinguish clusters with  $\delta$ -electrons from events with low angles between trajectories, where currently two physical clusters are merged into one. In the same way, no significant time information can be extracted in the pileup case, where amplitude samples in single strips are influenced by more than one crossing particle.

One possibility to achieve this may be given in the correlation between cluster amplitudes in adjacent planes (Fig. 7.1). The amplitudes from both planes in a single module are

## 7 CONCLUSION

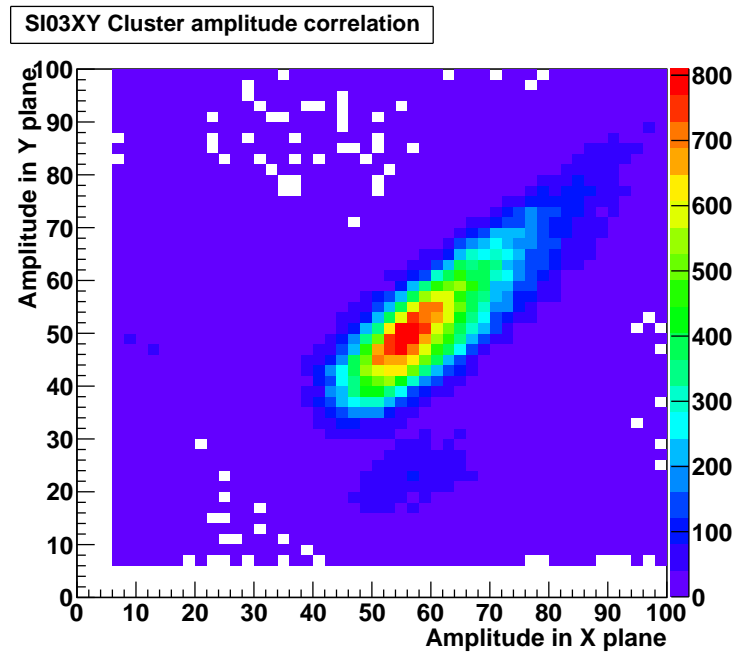


**Figure 7.1:** Cluster amplitude correlation between hits in SI03X and SI03Y, belonging to the same track. Data was taken from run 76860 (hadron run 2009)

known to be equal within the noise margins for hits belonging to the same particle. This could be used to disentangle pileup and merging of neighbouring clusters, but, apart from technicalities on the programming side, also thorough studies of the effects will be necessary.

# Appendix A

## Time calibration guide

This chapter deals with the technical details of the time calibration process. For description of the actual time reconstruction, consult section 4.2 (This is strongly recommended if you have no idea about time calibration so far).

The calibrations are stored in a text file for every single plane, which is of the format

$$\begin{array}{cccccccc} t_{lin,00} & t_{lin,01} & m_0 & m_1 & t_{c,0} & t_{c,1} & & \\ r_{0,min} & r_{0,max} & r_{00} & t_{00} & a_0 & c_0 & b_0 & d_0 \\ r_{1,min} & r_{1,max} & r_{01} & t_{01} & a_1 & c_1 & b_1 & d_1 \end{array}$$

with the parameters in the first line being from an outdated time reconstruction method with a simple linear function

$$(A.1) \quad r_i = t_{lin,0i} + m_i t - t_{c,i}$$

and the second and third line consisting of the parameters for the actually used reconstruction method. The first two parameters here are used only in the online filter and constitute limits within which the ratios need to lie in order for time calibration to be done. The remaining parameters in the second and third line are described in 4.2.

Obviously, the last two parameters in the first line are unnecessary since their property is actually the same as that of the  $t_0$ . Consequently, their value has been zero for all calibrations after 2002. In the process of this thesis, they were redefined to also be the value of the time correction by cluster size for the new reconstruction function (by shifting the  $t_0$  of the linear functions by the same value, no damage is done to the linear calibration in case it is ever used again)

All files necessary for time calibration are described below and are available in an SVN repository on `/afs/e18/compass/silicon/trunk/phzimmer/` or in separate

repositories on CERN machines (in case of commonly used software, e.g. Coral or cinderella).

### A.1 Raw data

Raw data is stored in *chunks* of about 1 GB in size on CASTOR, the CERN tape storage (cf. sect. 2.3.1, which can be accessed via `lxplus`. Operating on CASTOR works slightly different than on the usual hard drive devices:

- You can not `cd` into a folder, but you can list it via `ns ls <path>`
- You can not instantaneously access a file, you have to request it first via `stager_get -M <path to file>`
- Check whether the requested file has been prepared ("staged") yet via `stager_qry -M <path to file>`
- If so, you can copy it using `rfcop <path to file> <destination>` or streaming it (i.e. get text output) via `rfcats`

The standard procedure is to either copy the file to a `/tmp/` directory and to `scp` it from there to your local machine, or to directly stream it through a `ssh` channel. There are scripts available at E18 for both methods. Raw data from COMPASS is available in

`/castor/cern.ch/compass/data/<year>/raw/`,

or rather in the subdirectories named according to the respective data taking period.

### A.2 Coral and PHAST

Available as a CVS repository at CERN, but may be switched to another system soon since CERN will stop supporting CVS in the potentially near future. For information on how to check out and compile Coral, PHAST and its `coral.exe`, consult the E18 Wiki, site "Coral and PHAST at E18". Once you have compiled your `coral.exe`, you still need to modify an option file so it suits your needs. Take the standard option file for the period for which you want to calibrate (i.e. `$CORAL/src/user/trafdic.2009.primakoff.opt`), create a copy to work with and set/change the options you wish to use. A set of potentially useful options is given in the following list:

- `mDST file <file path and name>` : Define output mDST file path - e.g. `$HOME/phast.mDST`
- `mDST select <value 0-9>` : Define triggers to be used - 0: use all events

- Data file `<path>` : Path to input raw file
- CDB server `mysql` : E18's MySQL server - `mysql` (for E18), `compass02` (on lx-plus)
- CDB specialplace `MUNICH` : Take calibrations from E18 file system
- SI TimeCalibMunich `<setting>` : Get SI time calibrations from special folder - settings: `on`, `off`, `<string>`. The time calibrations for silicon detectors will be taken from `"/afs/e18/compass/silicon/timecalib/timingfiles/"` - this option should be used to test newly created calibrations before checking them in
- TraF `iCut [20] <value>` : min. # of SciFi hits in beam telescope
- TraF `dCut [77-78] <value> <value>` : time cuts for silicons (sigmas, nanoseconds) - set high (e.g. 100 sigmas, 1000ns) if available calibrations are very far off
- TraF `dCut [79] <value>` : Si time error rescaling factor - again, set high if calibrations are far off. This is set to 3 by default for most years, if your time calibrations for one whole year are complete (and good), ask the COMPASS analysis coordinators to change this.
- TraF `Graph [0] <0,1>` : Switch on/off event display - off (0) for actual runs, on (1) for test (wether Coral actually works)
- `mDST Hits SI` : store hit information for silicons - necessary for time calibration
- `mDST DAQdigits SI` : store raw digits for silicons - necessary in latency scan, potentially useful while calibrations are still bad.

Once the option file is successfully modified, you can start coral in your `$PHAST/coral` directory by typing

```
./coral.exe <path to your option file>.
```

The tracking process will usually take several hours and use a lot of computing resources (i.e. one full processor, if available), so you may want to consider:

- running it on the batch system
- running it in a screen session, re-nice'd<sup>1</sup>
- running overnight

The result of this job will be a `mDST` file, containing information about all processed events, with tracks and hits correlated to those tracks.

---

<sup>1</sup>read manpages for `screen`, `nice` and `nohup` for further information, `man screen` etc. in the command line

### A.3 PHAST user event functions

To make use of this information, we will need to write the event-by-event data to (event-independent) histograms. This is done with PHAST and a self-written user event function. When executing PHAST with such a user event function, it will go through every single event in the mDST file and perform the actions specified in the function for each event. For time calibration, there is a file named "UserEvent18.cc" available in the before-mentioned SVN repository. Place it in your \$PHAST/user/ directory and (re-)compile PHAST. After that, you will be able to execute PHAST by typing

```
./phast -u18 <path to input mDST file> (-h <path for output root file>) (-o <path to output mDST file>)
```

The -h option is optional, if omitted, the file will by default be written to \$PHAST/hist.root. The '-u18' option explicitly calls the UserEvent18 function. The '-o' option is not of any use in this special case but is essential for actual physics analysis, where PHAST is used mostly to apply cuts to events. Only events on which the `PaEvent::TagToSave()` method is called will be written to the output mDST file.

The output root file for UserEvent18 will contain several histograms for each detector plane, displaying time for a hit with respect to the corresponding track time, track time with respect to the event's TCS phase, hit times sorted by cluster size, the "banana plot" ( $r_0$  vs.  $r_1$ ) and  $r_0/r_1$  vs. TCS phase. Among these, the most important histograms for time calibration are the hit time (w.r.t. track time) for simply finding shifts in timing, and the ratio vs. TCS phase histograms for determining the actual shape (and thus the parameters) of the reconstruction function.

#### Signal shape and latency scan

In case you need to determine all reconstruction parameters (usually at the start of a runtime), a latency scan is practically indispensable for a good time calibration. Information on when the latency scan was performed can be taken from the run logbook. On Coral level, all you need to change is to activate writing of the DAQ digits for silicons in the option file. On PHAST level: In UserEvent18.cc, simply comment/uncomment wherever the file says so, and recompile. Now you can run PHAST with several mDST files from all runs belonging to a latency scan (sorted by latency settings, rising). This way, the ratio vs. TCS phase and the banana plot histogram are filled with all DAQ digits (taking into account the evolving latency settings), however the other histograms are not filled. In the ratio vs. TCS phase plots, the whole signal shape over several clock cycles is now visible - This is essential for determining the right reconstruction parameters.

## A.4 Root macros and creating/editing calibrations

If not indicated differently, the root macros in this section use the root files created with PHAST and UserEvent18.cc.

### Signal shape

The macro "TimeCalibration.cc", written by Jörg Martin in 2009, is a useful tool to create calibrations by hand - there is actually an auto-calibration framework by A.-M. Dinkelbach, however the results of this software are usually not optimal and a better calibration can be created by hand.

Currently, the root file to be used has to be defined inside the file (this will be changed...). Also, calibrations (or pseudo-calibrations containing the necessary amount of parameters) need to be available in the folders "calculated\_calibration" and "changed\_calibration". When starting, the macro will prompt for the station and plane that you wish to create/edit a calibration for, then for the latency setting of the specified file - by entering 0 here you can see the whole area. After that, there are several options what to do:

- Draw the histograms and the graphs for the "old" parameters
- Draw the histograms and the graphs for the changed parameters
- Change the value of one or several parameters in the reconstruction function
- Overwrite the "old" parameters with the changed parameters
- Restore the "old" parameters into the changed parameters

Basically, it's sufficient to work with only the changed parameters, the "old" configuration serves only as a backup of potentially good parameter sets. Change the parameters in a way so they fit the signal shape well. A rough set of parameters to start of with may be:

(A.2)	$a_0 = 0.05$	$a_1 = 0.05$
(A.3)	$b_0 = 5$	$b_1 = 8$
(A.4)	$c_0 = 0.08$	$c_1 = 0.09$
(A.5)	$d_0 = -0.2$	$d_1 = -0.4$
(A.6)	$r_{00} = 2.25$	$r_{01} = 1.5$
(A.7)	$t_{00} = 25.7$	$t_{01} = 0$

The parameter  $r_0$  defines the maximum value of the ratio, while  $t_0$  leaves the shape intact and shifts it along the time axis.  $a$  and  $c$  make the major contribution to the slope in

## A TIME CALIBRATION GUIDE

the early and the late part of the signal, respectively, while  $b$  is most useful to define the "bend" in the middle of the rising signal. The  $d$  parameter can be used to change the "foot point" of the shape, i.e. define where the ratios start to rise from zero without shifting the complete shape.

The values of  $t_0$  can vary wildly, depending on factors like the length of the fiber cable between the ADC card and the GeSiCA. There are some constraints one should pay attention to, because though they are not crucial to a good time reconstruction, they hold within them an inner consistency to the calibrations that is not very easy to find otherwise.

$$(A.8) \quad r_{00} = r_{01}^2$$

$$(A.9) \quad t_{00} = t_{01} + \Delta, \quad \Delta = 25.7\text{ns}$$

The constraint for the maximum ratios arises from the exponential decay of the signal towards the end, coupled with the fact that  $t_2 - t_0 = 2(t_2 - t_1) = 2\Delta$ , while the constraint on the time shift is based solely on  $t_1 - t_0 = \Delta$ .

### "Bonus round": Verifying the signal shape

The signal shape macro by A.-M. Dinkelbach is a nice way to check the consistency of your calibration: It reconstructs the actual amplitude from the calibrations. Since each ratio is on its own sufficient to do this, we end up with two independent signals. When superimposing these curves, the area they enclose can be understood as a measurement of the consistency of the calibrations for the two ratios.

By default, the macro uses the calibrations from the "changed\_calibration" folder and creates .eps files displaying both ratio curves and the two reconstructed amplitude shapes superimposed. If you want to check for other calibrations, replace the list in the beginning of "si\_amp\_20091007.C" in an appropriate way (i.e. adjust the array size and replace the file names). After that, in root, compile APV\_timing.cc (.L APV\_timing.cc) and execute si\_amp\_20091007.C (.x si\_amp\_20091007.C).

### Shifting $t_0$

Once you have determined the signal shape of all planes, the longer (but also more interesting) part of the work is done. What is left is shifting the  $t_0$  so the timing histogram peaks at zero. Using the new calibrations, produce a run with Coral (Silicon hits required, but no DAQ digits) and make timing histograms with user event 18 (standard, not latency scan mode). The root macro "Multigauss.cc" will, taking the path to this rootfile as an argument, fit a gaussian to the peak and, taking the calibrations from the "changed\_calibration" folder, change the  $t_0$  values by the mean of the gauss and write the

new calibration into a separate folder. If you have rootfiles from several runs (produced with the same calibration), where all timings do not seem to vary a lot, you can as well use "Multigauss2.cc", which takes as an argument a file which contains a list of all rootfiles you wish to use. The histograms will be added up and then fitted, from then things will work just the same way as before.

In some tough cases, it may be necessary to iterate the shifting process several times, each time producing several thousand events in Coral with the new iteration of calibrations.

### **Ready for Check-in?**

Now that you have created valid calibrations (congratulations!), you only need to check them in to the COMPASS database. For this, the file names will have to be changed first, including the type of calib and validity time range. The correct format of any calibration you want to check in is

```
<TBName><typecalib>~~start-YYYY-MM-DD-HH:MM:SS~~finish-YYYY-MM-DD-HH:MM:SS
```

i.e. in our case like:

```
SI01U1__timing~~start-2009-01-01-00:00:00~~finish-2009-12-31-23:59:59
```

As validity range, choose:

- **First calibration:** When creating the first (proper) calibration of the year, choose the time range as in the example above.
- **During run:** Otherwise, the start time should be equal to the (start) time of the first run that this calibration was created with. If you are still within the same year as data taking, choose the end time as above.
- **Later:** If the run is already completely over, create calibrations only with specific time ranges, from the beginning of a run to the beginning of another run.

There are several shell scripts available suited for this purpose, for exact usage read their commentary. Once the file names are set correctly, log in to the COMPASS gateway (tunneling through lxplus). If you do not have a CERN computing account, ask somebody to log in for you (and also, think about registering as an external member so you can get a computing account). Get an afs token using "klog <username>@cern.ch" and copy the the calibration files to a place accessible from the gateway (e.g. /online/detector/silicon/<year>/time\_calib/). Check in the files with "loadOldFileInDB <path to calib file(s)>" - use \* as a wildcard. The password you need is one of the two standard COMPASS passwords, the same as for the run logbook (if you do not know the password, ask somebody again)

## A TIME CALIBRATION GUIDE

After that, calibrations are available in the database. In order for the calibrations to be usable in the E18 network, they still need to be copied back to the E18 afs calibration folder. This is automatically done every night, if you need them right away, ask your admin to start this synchronisation (it will take a few minutes). Until this synchronisation is done, you will not be able to run a Coral job with data from the time period for which you checked in calibrations since the database will already give paths to the new calibration files, even though they are not available yet. It is, however, possible to use local calibrations by specifying `SI TimeCalibMunich on` in the option file.

## Appendix B

# Plots and Histograms

SI02X was the casualty of an accident in september 2009 and it was not usable afterwards, thus the histograms are omitted.

For SI03X and SI04U, pseudo-efficiencies turn out to always be 100 %, as the planes define the tracks that enter and exit the target.

## SI01UV

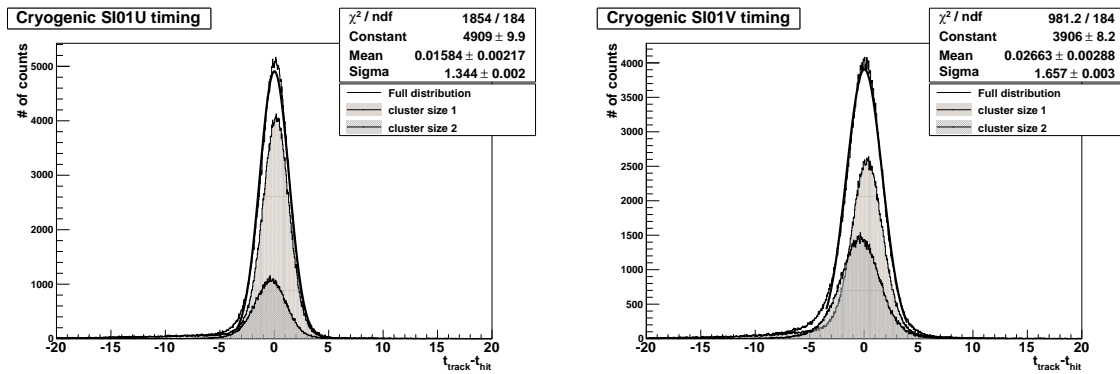


Figure B.1: Timing in run 81811 with cluster size correction

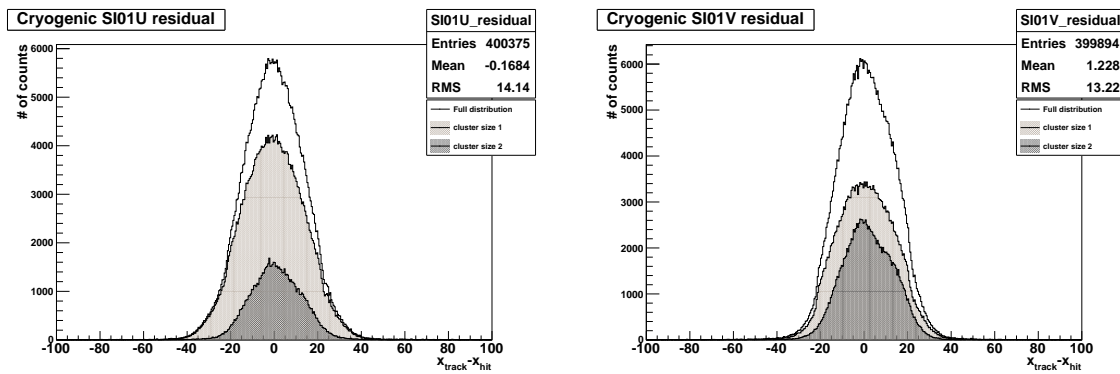


Figure B.2: Residual distribution for run 81811

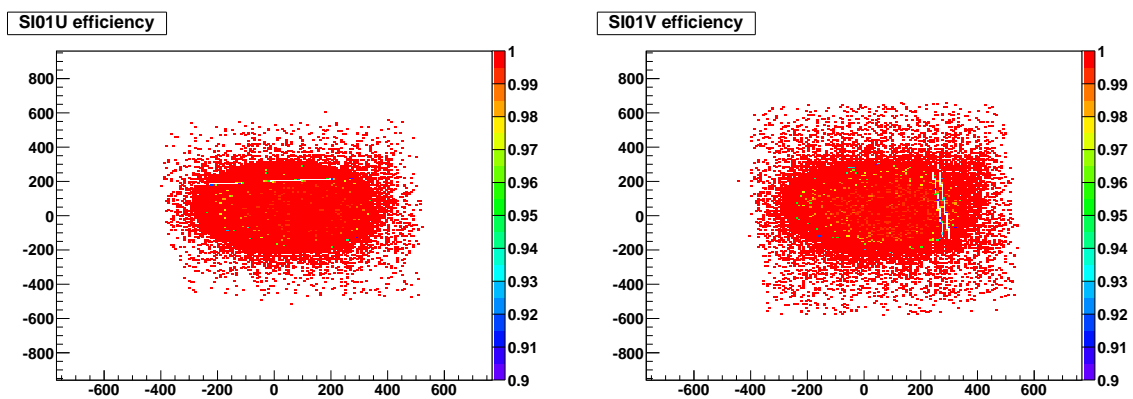


Figure B.3: SI01UV efficiencies for run 81811

# SI01XY

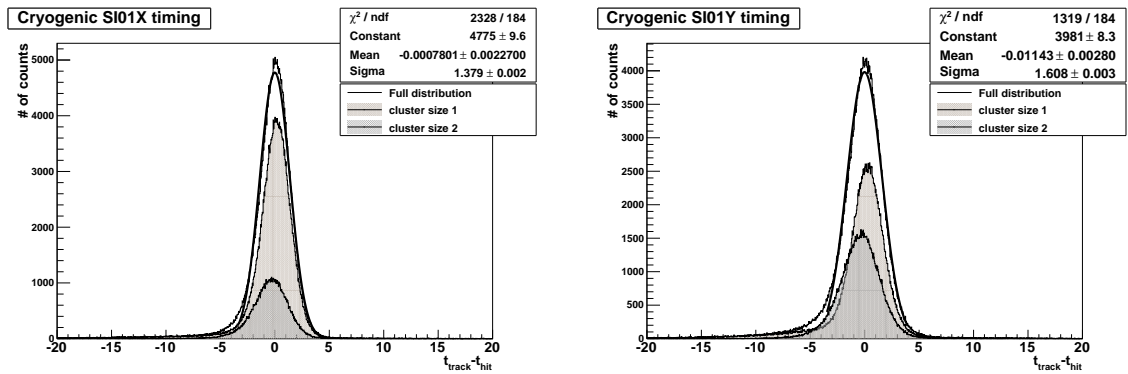


Figure B.4: Timing in run 81811 with cluster size correction

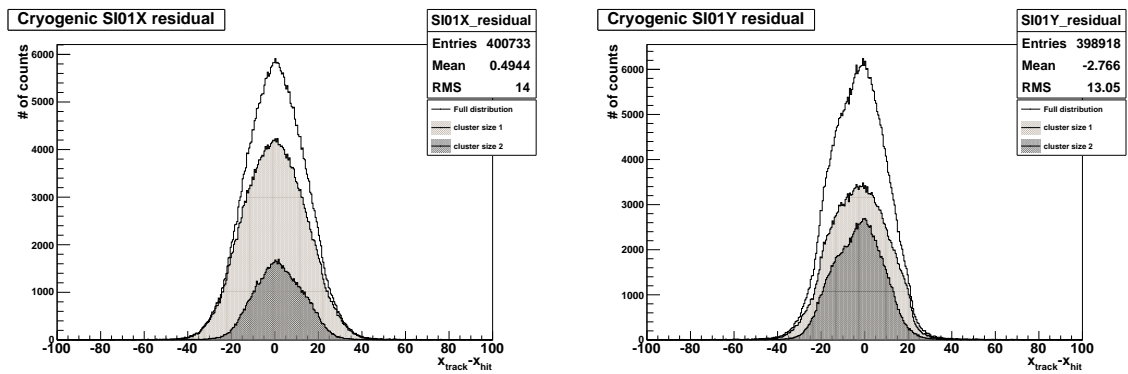


Figure B.5: Residual distribution for run 81811

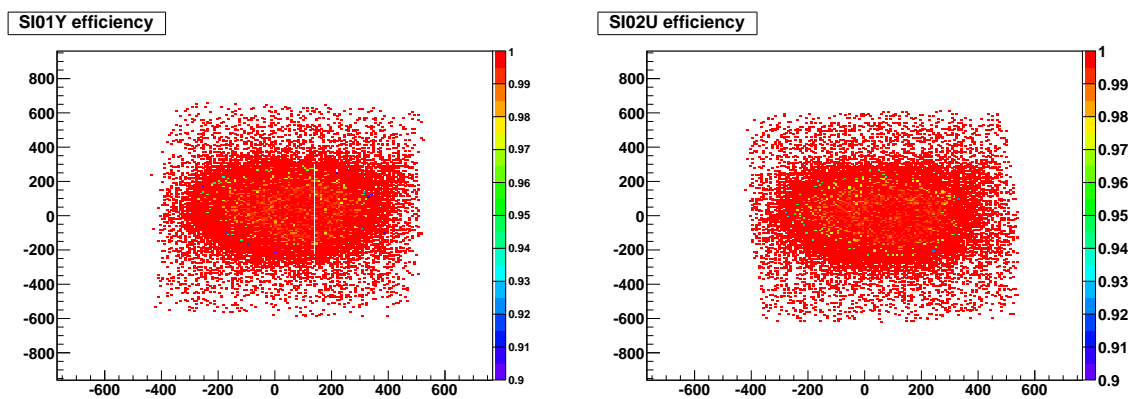


Figure B.6: SI01XY efficiencies for run 81811

## SI02UV

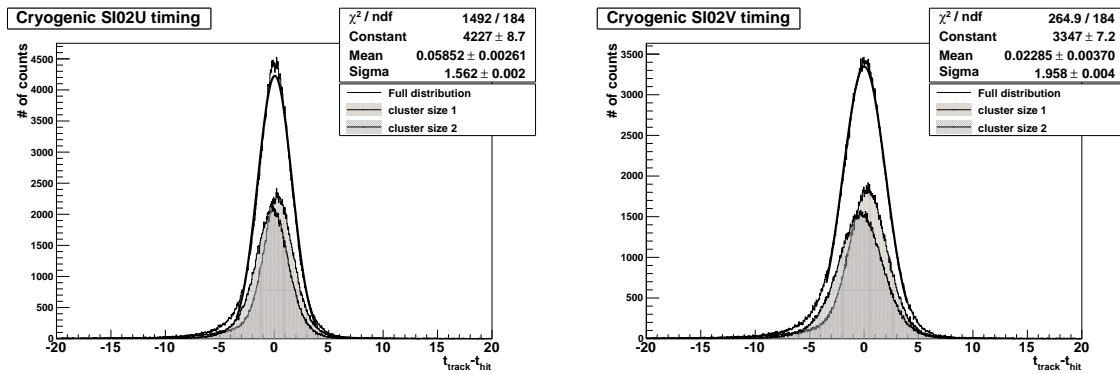


Figure B.7: Timing in run 81811 with cluster size correction

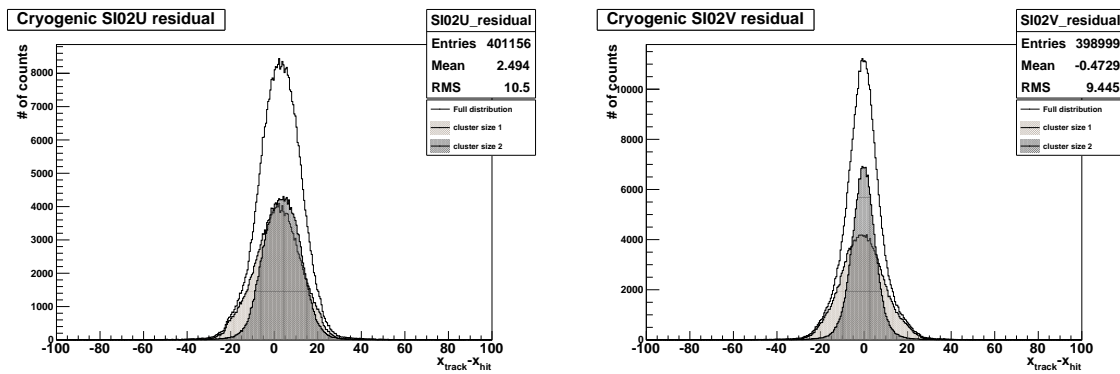


Figure B.8: Residual distribution for run 81811

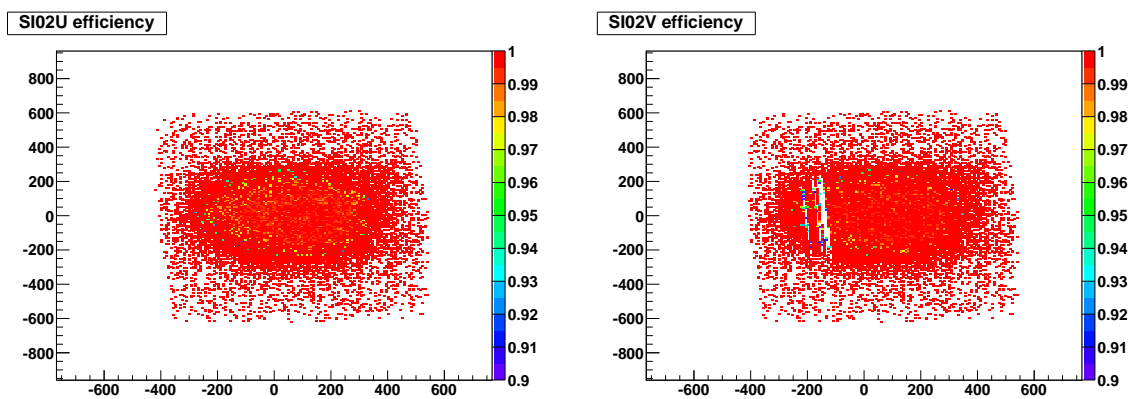


Figure B.9: SI02UV efficiencies for run 81811

# SI02Y

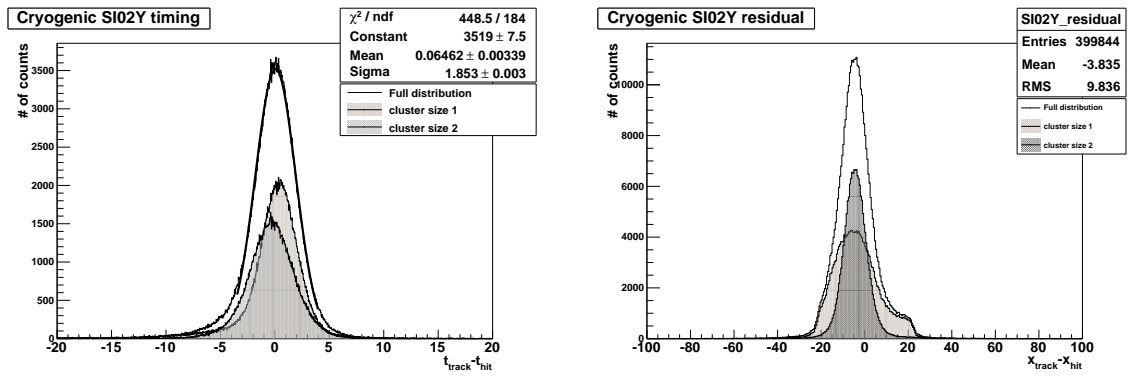


Figure B.10: Timing and residual for SI02Y in run 81811

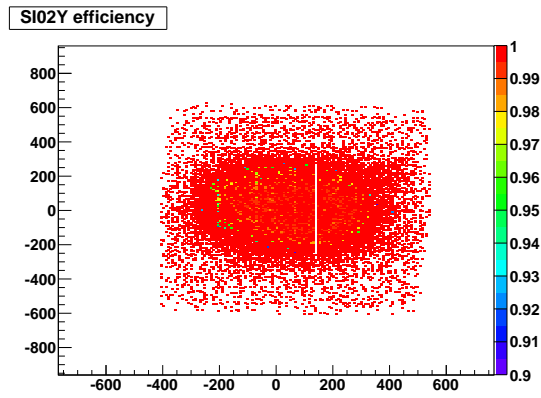


Figure B.11: SI02Y efficiency for run 81811

SI03UV

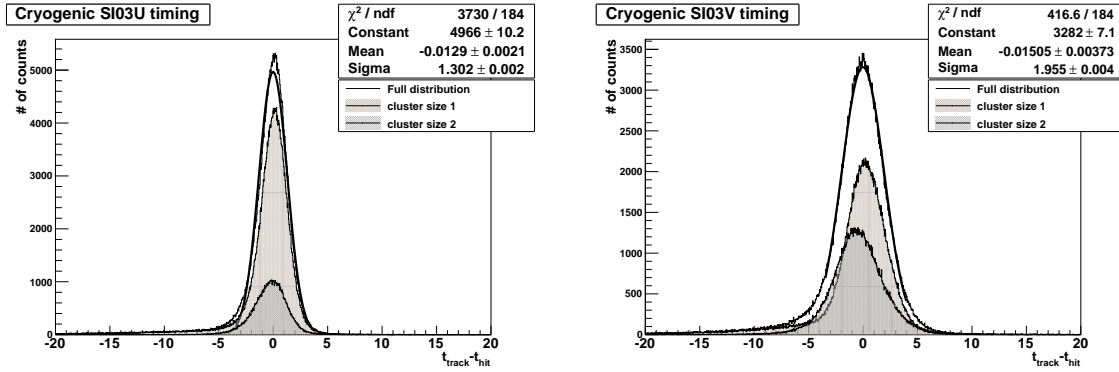


Figure B.12: Timing in run 81811 with cluster size correction

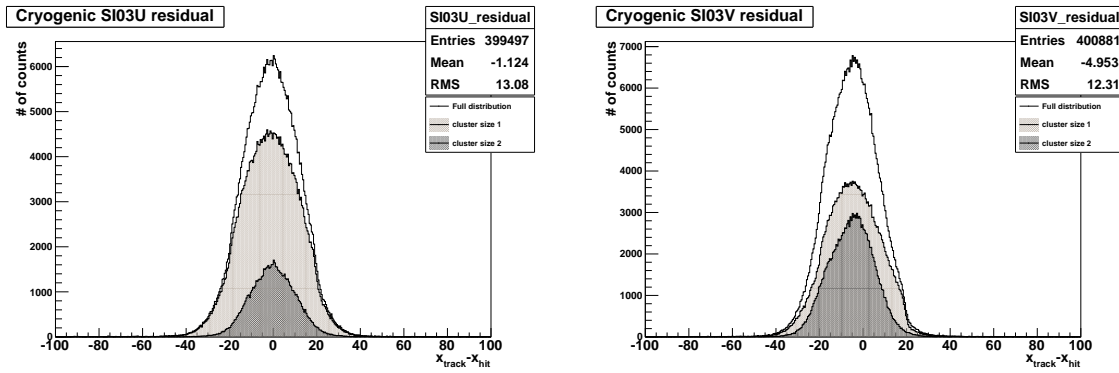


Figure B.13: Residual distribution for run 81811

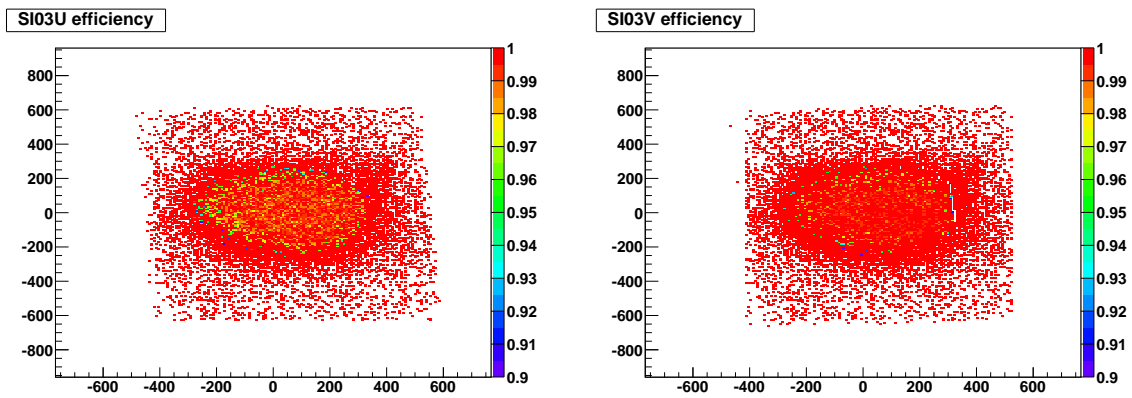


Figure B.14: SI03UV efficiencies for run 81811

# SI03XY

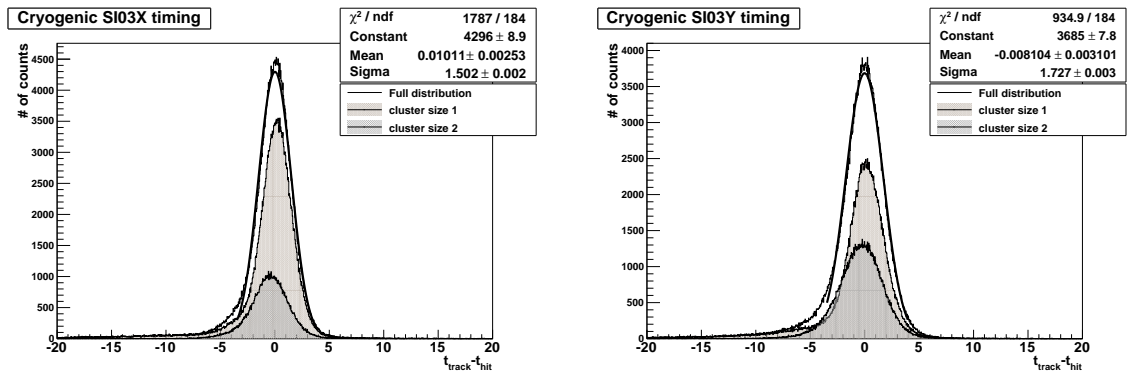


Figure B.15: Timing in run 81811 with cluster size correction

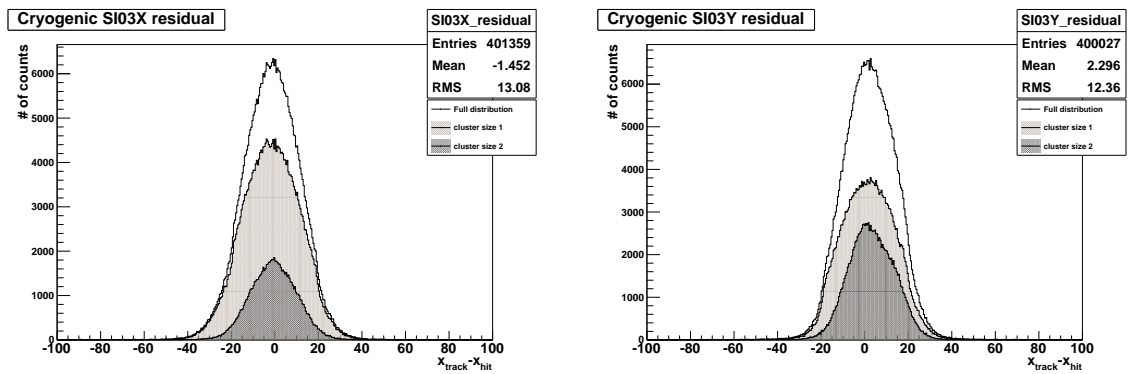


Figure B.16: Residual distribution for run 81811

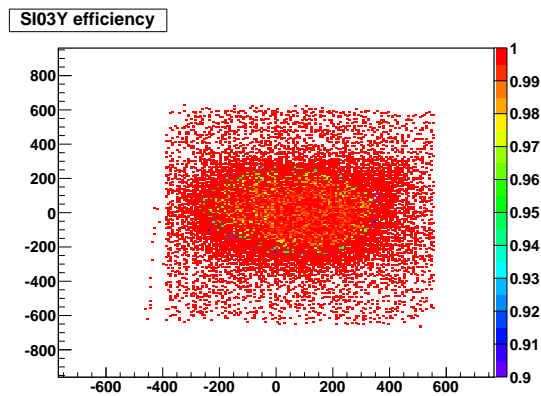


Figure B.17: SI03Y efficiency for run 81811

## SI04UV

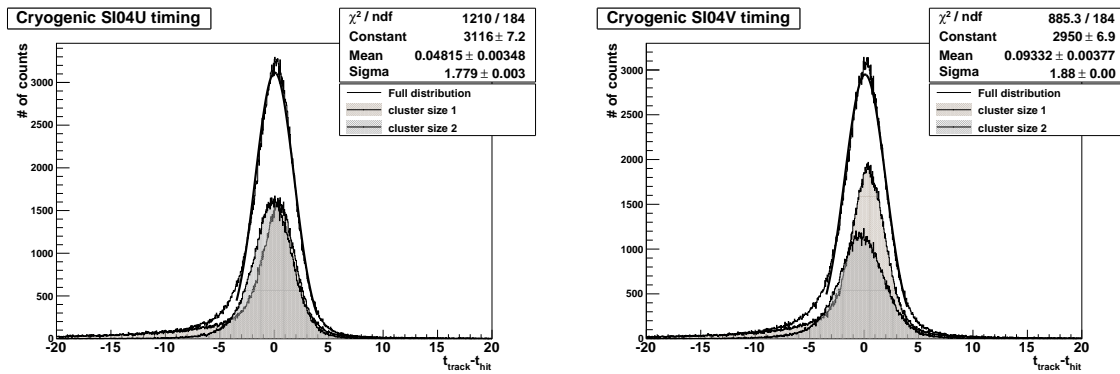


Figure B.18: Timing in run 81811 with cluster size correction

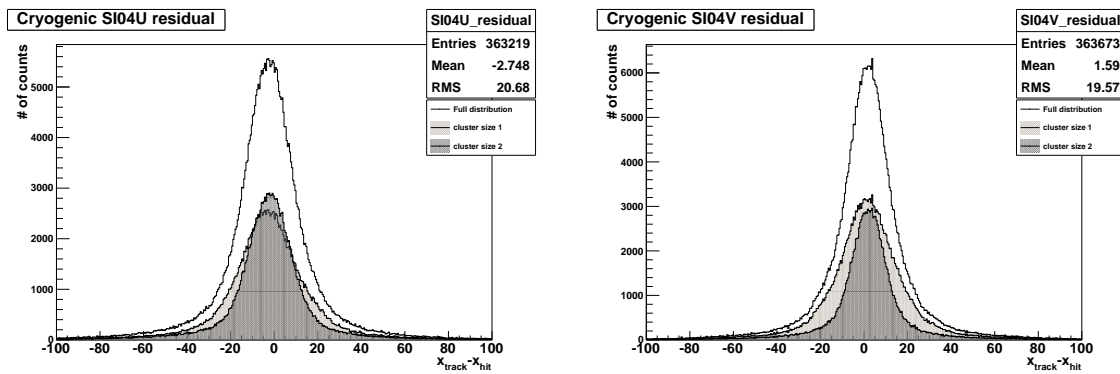


Figure B.19: Residual distribution for run 81811

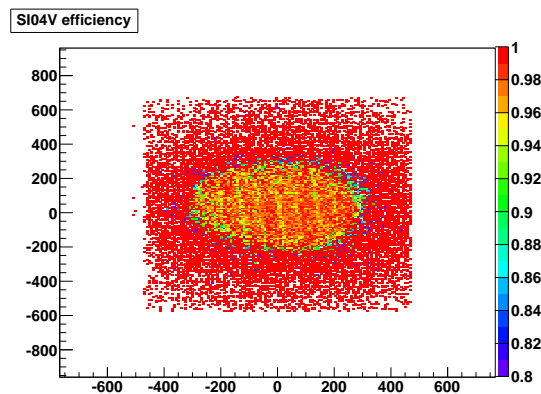


Figure B.20: SI04V efficiency for run 81811

# SI04XY

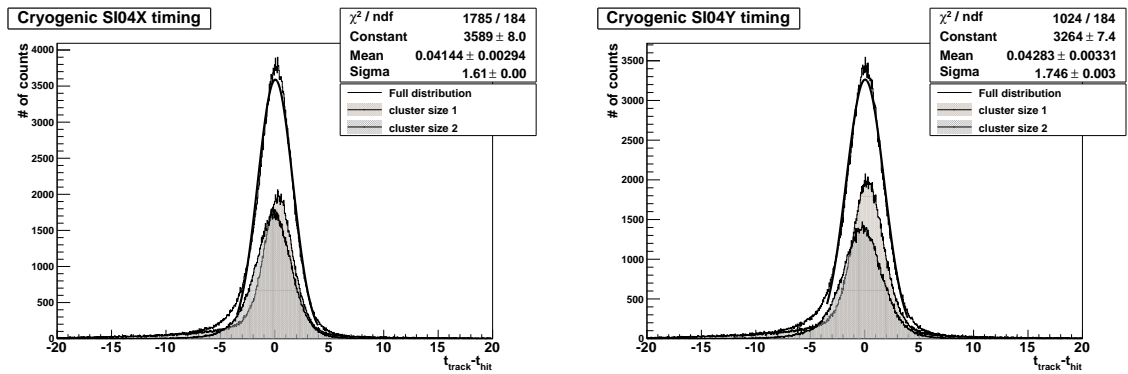


Figure B.21: Timing in run 81811 with cluster size correction

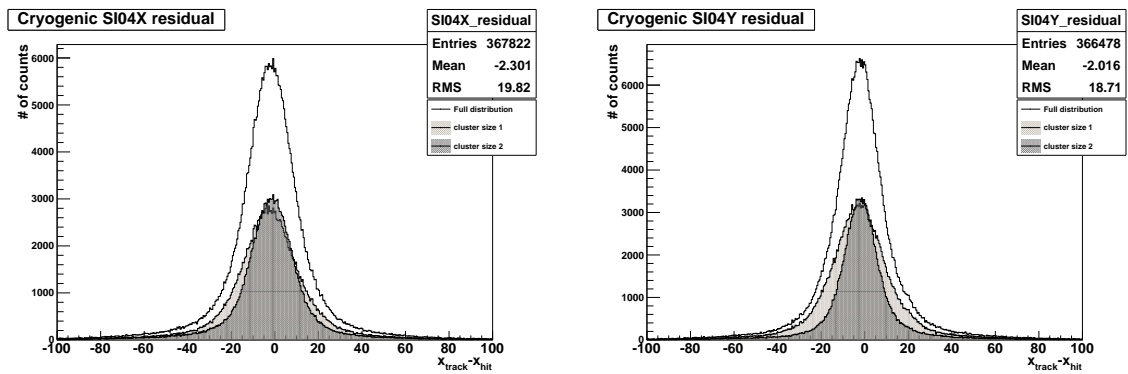


Figure B.22: Residual distribution for run 81811

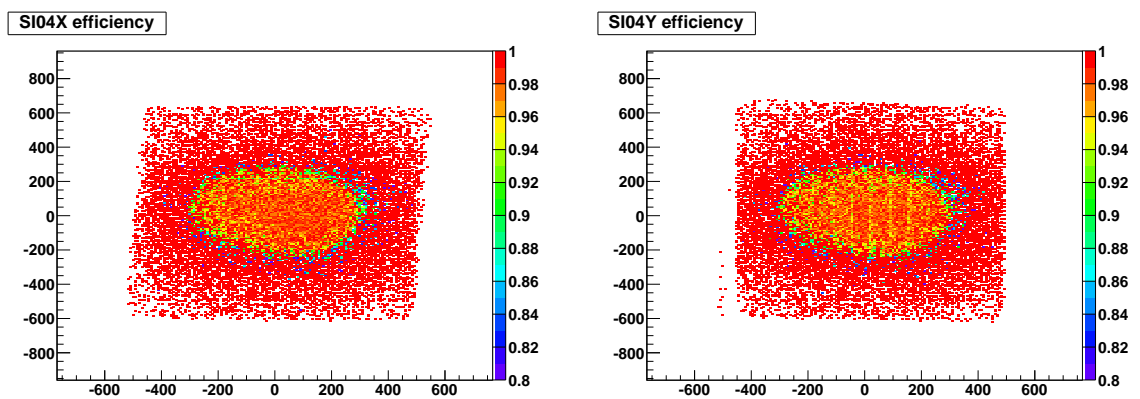


Figure B.23: SI04XY efficiencies for run 81811

## SI05UV

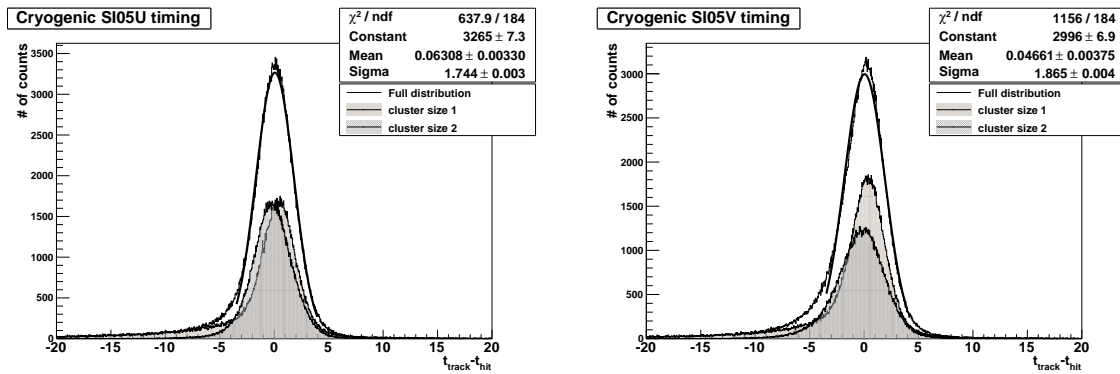


Figure B.24: Timing in run 81811 with cluster size correction

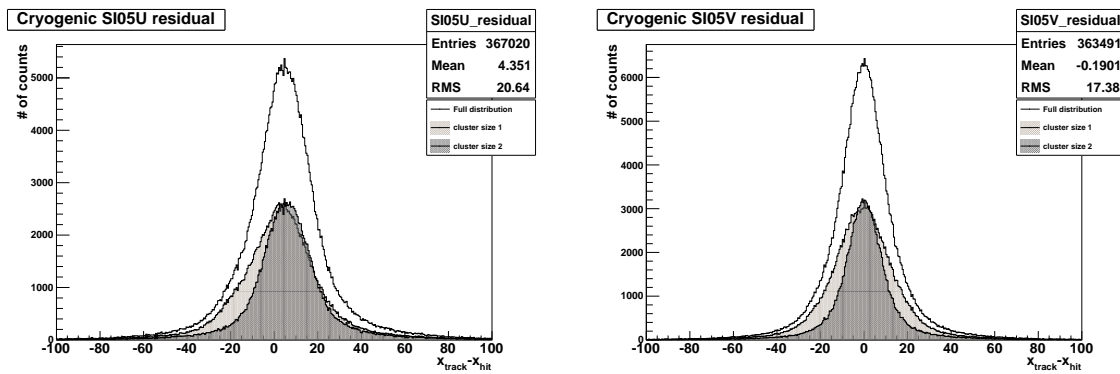


Figure B.25: Residual distribution for run 81811

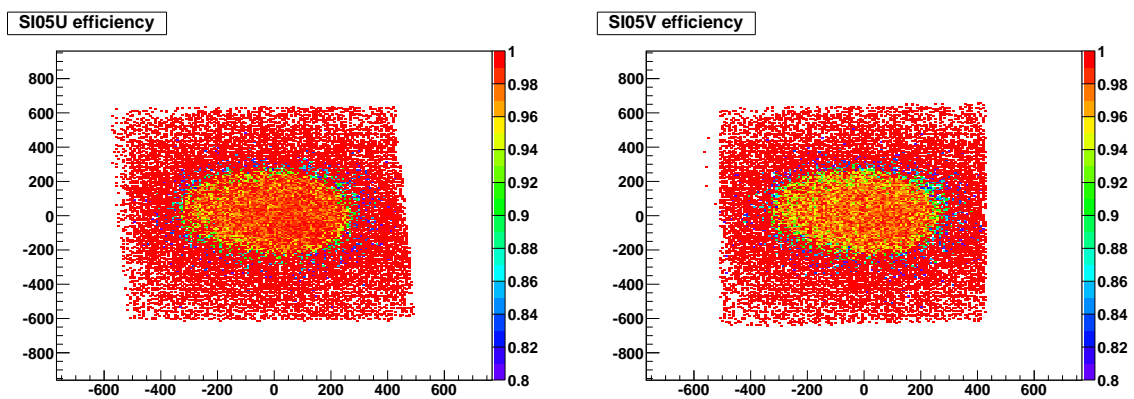


Figure B.26: SI05UV efficiencies for run 81811

# SI05XY

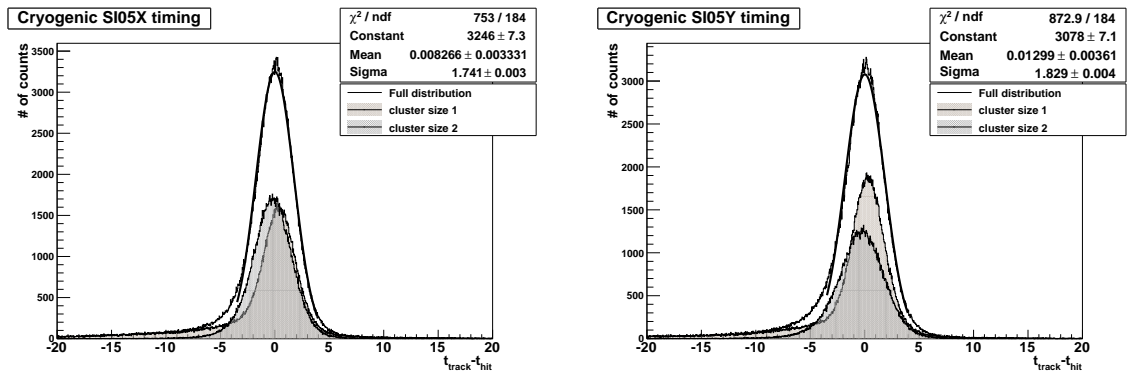


Figure B.27: Timing in run 81811 with cluster size correction

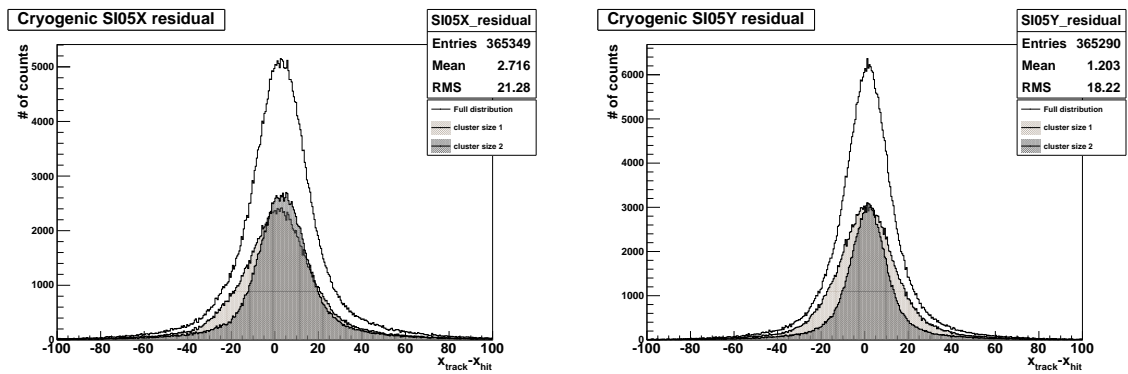


Figure B.28: Residual distribution for run 81811

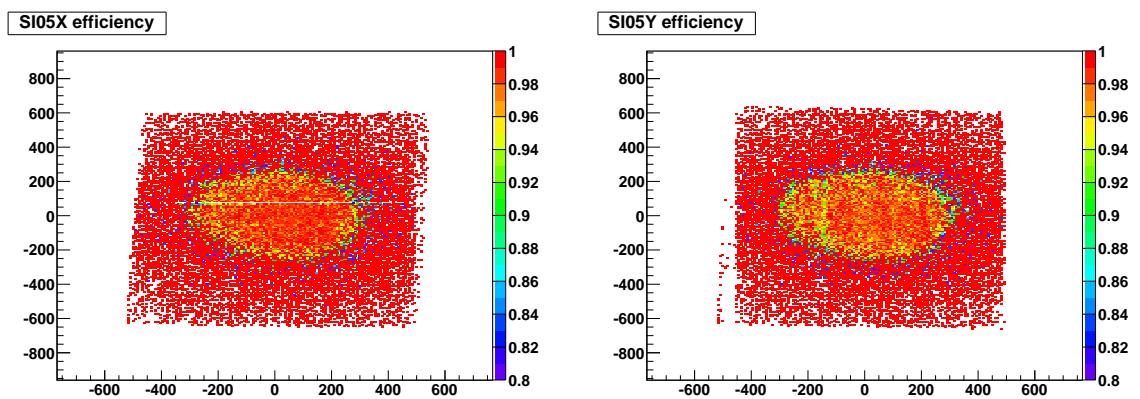


Figure B.29: SI05XY efficiencies for run 81811



# Bibliography

- [Abt96] I. Abt et al. Irradiation tests of double-sided silicon strip detectors with a special guard ring structure. *IEEE Trans. Nucl. Sci.* **43**, 1113–1118 (1996).  
(Cited on page 19.)
- [Aus10] Alexander Austregesilo, . Private communication, 2010. (Cited on page 53.)
- [Bic11] K. Bicker. *Construction and commissioning of a cooling and support structure for the Silicon Detectors for the COMPASS experiment*. Diploma thesis, Technische Universität München, January 2011. (Cited on pages V, 24, 25, and 26.)
- [CAS] CASTOR. Home page, <http://castor.web.cern.ch>. (Cited on page 13.)
- [Co96] The COMPASS collaboration. A proposal for a Common Muon and Proton Apparatus for Structure and Spectroscopy. *CERN SPSLC 96-14* (1996).  
(Cited on page 3.)
- [Col89] The EMC Collaboration. An investigation of the spin structure of the proton in deep inelastic scattering of polarised muons on polarised protons. *Nuclear Physics B* **328 1**, 1 – 35 (1989).  
(Cited on page 6.)
- [COM] COMgeant: COMmpass monte carlo simulation program based on geant3, <http://valexakh.web.cern.ch/valexakh/wwwcomg/index.html>.  
(Cited on page 13.)
- [COM05a] The COMPASS collaboration. Measurement of the spin structure of the deuteron in the dis region. *Physics Letters B* **612**, 154–164 (2005).  
(Cited on page 5.)
- [COM05b] The COMPASS collaboration. Search for the  $\phi(1860)$  pentaquark at compass. [oai.cds.cern.ch:828557](http://oai.cds.cern.ch:828557). *Eur. Phys. J. C* **41 hep-ex/0503033**. **CERN-PH-EP-2005-009**. **DAPNIA-2005-29**, 469–474. 10 p Mar 2005. (Cited on page 5.)
- [COM06] The COMPASS collaboration. Gluon polarization in the nucleon from quasi-real photoproduction of high-pT hadron pairs. *Physics Letters B* **633 1**, 25–33 February 2006. (Cited on page 6.)
- [COM07a] The COMPASS collaboration. The COMPASS experiment at CERN. *Nucl. Inst. Meth. A* **577**, 455–518 (2007). (Cited on page 8.)

## BIBLIOGRAPHY

- [COM07b] The COMPASS collaboration. The deuteron spin-dependent structure function  $g_1^d$  and its first moment. *Physics Letters B* **647**, 8–17 (2007). (Cited on page 5.)
- [COM07c] The COMPASS collaboration. A new measurement of the collins and sivers asymmetry on a transversely polarized deuteron target. *Nuclear Physics B* **765**, 31–70 (2007). (Cited on page 6.)
- [COM07d] The COMPASS collaboration. Spin asymmetries  $A_1^d$  and the spin-dependent structure functions  $g_1^d$  of the deuteron at low values of  $x$  and  $Q^2$ . *Physics Letters B* **647**, 330–340 (2007). (Cited on page 5.)
- [COM08] The COMPASS collaboration. The polarised valence quark distribution from semi-inclusive DIS. *Physics Letters B* **660**, 458–465 (2008). (Cited on page 5.)
- [COM09a] The COMPASS collaboration. Collins and Sivers asymmetries for pions and kaons in muon-deuteron DIS. *Physics Letters B* **673**, 127–135 (2009). (Cited on page 6.)
- [COM09b] The COMPASS collaboration. Flavour separation of helicity distributions from deep inelastic muon-deuteron scattering. *accepted by Physics Letters B CERN-PH-EP/2009-008, arXiv:0905.2828v1* (2009). (Cited on page 5.)
- [COM10a] The COMPASS collaboration. COMPASS-II Proporsal. *CERN-SPSC-2010-014 ; SPSC-P-340* (2010). (Cited on pages 11, 12, and 24.)
- [COM10b] The COMPASS collaboration. Observation of a  $j^{PC} = 1^{-+}$  exotic resonance in diffractive dissociation of  $190 \text{ gev}/c \pi^-$  into  $\pi^- \pi^- \pi^+$ . *Phys. Rev. Lett.* **104** **24**, 241803 Jun 2010. (Cited on page 5.)
- [Din11] A.-M. Dinkelbach. *Precision Tracking and Electromagnetic Calorimetry towards a Measurement of the Pion Polarisabilities at COMPASS*. Phd thesis, Technische Universität München, January 2011. (Cited on pages V, 17, 21, 35, 38, and 40.)
- [EDM] EDMS home page, <http://edms.cern.ch>. (Cited on page 51.)
- [Fri10] Jan Friedrich, . Private communication, 2010. (Cited on page 31.)
- [Gra11] S. Grabmüller. *PhD thesis in preparation*. Phd thesis, Technische Universität München, May 2011. (Cited on page 23.)
- [Gru01] B. Grube. *The Trigger Control System and the common GEM and Silicon Read-out for the COMPASS Experiment*. Diploma thesis, Technische Universität München, December 2001. (Cited on page 29.)
- [Jon] L. L. Jones et al. The APV25 deep submicron readout chip for CMS detectors. . Prepared for 5th Workshop on Electronics for the LHC Experiments (LEB 99), Snowmass, Colorado, 20-24 Sep 1999. (Cited on page 20.)
- [Leo94] W. R. Leo. *Techniques for nuclear and particle physics experiments*. Springer, 1994. (Cited on page 17.)

- [Log] COMPASS run logbook, <http://wwwcompass.cern.ch/RunLogbook/diirphp/>. (Cited on pages 31 and 51.)
- [Mar09] Jörg Martin. Time calibration for the silicon detectors of the COMPASS experiment. August 2009. (Cited on page 36.)
- [Nag05] T. Nagel. *Cinderella: An Online Filter for the COMPASS Experiment*. Diploma thesis, Technische Universität München, January 2005. (Cited on page 13.)
- [Pal98] V. Palmieri et al. Evidence for charge collection efficiency recovery in heavily irradiated silicon detectors operated at cryogenic temperatures. *Nucl. Instr. and Meth. A* **413**, 475–478 (1998). (Cited on page 24.)
- [PDG10] Particle Data Group. Review of particle physics. *Journal of Physics G* **33**, 1 (2010). (Cited on page 29.)
- [Pei92] A. Peisert. Silicon microstrip detectors. *Adv. Ser. Direct. High Energy Phys.* **9**, 1–79 (1992). (Cited on page 17.)
- [Pug99] V. M. Pugatch et al. Radiation hardness of the HERA-B silicon microstrip detectors. *Nuovo Cim.* **112A** (1999). (Cited on page 19.)
- [ROO] R. Brun, F. Rademakers, et al. ROOT home page, <http://root.cern.ch>. (Cited on page 13.)
- [Sin97] R. W. Bernstein and T. Westgaard. Technical and test specifications for MPI HERA-B doublesided silicon. Technical report, SINTEF Electronics & Cybernetics, 1997. (Cited on page 18.)
- [SP95] W. Schmidt-Parzefall. HERA-B: An Experiment to study CP violation at the HERA proton ring using an internal target. *Nucl. Instrum. Meth. A* **368**, 124–132 (1995). (Cited on page 18.)
- [Spi05] H. Spieler. *Semiconductor Detector Systems*. Oxford Science Publications, 2005. (Cited on pages 17 and 29.)
- [Wag01] R. Wagner. *Commissioning of Silicon Detectors for the COMPASS Experiment at CERN*. Diploma thesis, Technische Universität München, December 2001. (Cited on pages V and 35.)
- [Wie04] M. Wiesmann. *A Silicon Microstrip Detector for COMPASS and a first Measurement of the transverse Polarization of  $\Lambda$ -Hyperons from quasi-real Photo - Production*. Ph.D. thesis, Technische Universität München, February 2004. (Cited on page 30.)



# Own contributions

This thesis was created within the framework of the chair of Prof. Stephan Paul at the Technische Universität München and at the COMPASS collaboration at CERN, Geneva.

Having become familiar with the silicon detectors during my year as a technical student at E18, my first task was to create a framework for time calibration and supply calibrations for the cryogenic detectors. In the process, I discovered the occurrence of synchronization problem between the TCS clock and the silicon readout, that was visible in the form of "jumps" by 12.8 ns in timing. With the support of Julian Taylor, I modified the on-line filter Cinderella to create calibrations (in offline mode) with the goal of compensating for those jumps, and implemented the use of these calibrations in Coral.

I investigated in properties of the silicon data, implementing a modification to time calibration to account for different cluster sizes and an improvisational modification for the splitting of large clusters.

I spent several weeks at CERN, supporting Karl Bicker in the setup of the silicon beam telescope for the 2010 beam time in april, taking shifts and on-call responsibilities in may and supporting Sverre Doerheim and Felix Böhmer in the setup of a spare silicon station in the test bench for the test-GEM-TPC in late august.

In late november, when issues and arguments concerning the alignment for 2009 data arose, I performed a rough investigation on the alignment of the silicon vertex detector along the z-axis, which initiated a do-over of the alignment procedure to improve data quality.



# Acknowledgements

## Thanks

to Stephan Paul for giving me the opportunity to work at COMPASS. It has been two very interesting and exciting years.

to Jan Friedrich, for being available basically at any time when I needed advice on any topic.

to Steffi Grabmüller, for introducing me to the silicons when I started at E18 and supporting me at any time.

to everyone (else) involved with the silicons, Charly Bicker, Michael Leeb, and all the technical students. It was fun working with you, both at CERN and in Munich.

to Julian Taylor, a great programmer who always knew how to help me out whenever anything did not work, for always being there and for helping me set up the online filter for use on lxbatch.

to Sebastian Uhl, who - it seems - knows just *everything* about COMPASS computing, for the many times he knew the answer to whatever question I came up with.

to "my" coffee crew for making even the worst days bearable thanks to the fun conversations in the E18 kitchen.

to Steffi Grabmüller, Charly Bicker, Jan Friedrich and especially Michael Leeb for proof-reading this thesis (or parts of it). Without you, it would have been a mess.

to Steffi, Charly, Alex and Stefan for sharing the office with me. It was just plain awesome, and every single one of you had a part in that.

to everyone who took part in our TV nights in the seminar room.

and basically to everyone at E18. I had a great time here, I always felt welcome and I will miss this environment.

to all my friends, for being there and being great over the last five years, for supporting me in bad times and for all the good times I had with all of you.

Ein Dankeschön an meine Familie, die jederzeit mit moralischer Unterstützung bereitstand und ganz besonders an meine Eltern, die mich über das ganze Studium finanziell unterstützt haben. Ohne euch wäre das alles nie möglich gewesen.